

## 4D synchrotron X-ray microtomography of fracture in nuclear graphite after neutron irradiation and radiolytic oxidation

Wade-Zhu, James; Krishna, Ram; Bodey, Andrew J.; Davies, Mark; Bourne, Neil K.; Rau, Christoph; Davies, Bruce; Tzelepi, Athanasia; Jones, Abbie N.; Marsden, Barry J.; Mummery, Paul M.

DOI:

[10.1016/j.carbon.2020.06.051](https://doi.org/10.1016/j.carbon.2020.06.051)

License:

Creative Commons: Attribution-NonCommercial-NoDerivs (CC BY-NC-ND)

*Document Version*

Peer reviewed version

*Citation for published version (Harvard):*

Wade-Zhu, J, Krishna, R, Bodey, AJ, Davies, M, Bourne, NK, Rau, C, Davies, B, Tzelepi, A, Jones, AN, Marsden, BJ & Mummery, PM 2020, '4D synchrotron X-ray microtomography of fracture in nuclear graphite after neutron irradiation and radiolytic oxidation', *Carbon*, vol. 168, pp. 230-244.  
<https://doi.org/10.1016/j.carbon.2020.06.051>

[Link to publication on Research at Birmingham portal](#)

### General rights

Unless a licence is specified above, all rights (including copyright and moral rights) in this document are retained by the authors and/or the copyright holders. The express permission of the copyright holder must be obtained for any use of this material other than for purposes permitted by law.

- Users may freely distribute the URL that is used to identify this publication.
- Users may download and/or print one copy of the publication from the University of Birmingham research portal for the purpose of private study or non-commercial research.
- User may use extracts from the document in line with the concept of 'fair dealing' under the Copyright, Designs and Patents Act 1988 (?)
- Users may not further distribute the material nor use it for the purposes of commercial gain.

Where a licence is displayed above, please note the terms and conditions of the licence govern your use of this document.

When citing, please reference the published version.

### Take down policy

While the University of Birmingham exercises care and attention in making items available there are rare occasions when an item has been uploaded in error or has been deemed to be commercially or otherwise sensitive.

If you believe that this is the case for this document, please contact [UBIRA@lists.bham.ac.uk](mailto:UBIRA@lists.bham.ac.uk) providing details and we will remove access to the work immediately and investigate.

# 4D Synchrotron X-ray Microtomography of Fracture in Nuclear Graphite after Neutron Irradiation and Radiolytic Oxidation

*J. Wade-Zhu<sup>af\*</sup>, R. Krishna<sup>a</sup>, A.J. Bodey<sup>c</sup>, M. Davies<sup>a,d</sup>, N.K. Bourne<sup>a</sup>, C. Rau<sup>c</sup>, B. Davies<sup>d</sup>, A. Tzelep<sup>e</sup>, A.N. Jones<sup>a</sup>, B.J. Marsden<sup>a</sup>, P.M. Mummery<sup>a</sup>*

*<sup>a</sup>Department of Mechanical, Aerospace & Civil Engineering, University of Manchester, Manchester, M13 9PL, UK.*

*<sup>b</sup>Henry Moseley X-ray Imaging Facility, School of Materials, University of Manchester, Manchester, M13 9PL, UK.*

*<sup>c</sup>Diamond Light Source, Oxfordshire, OX11 0DE, UK.*

*<sup>d</sup>EDF Nuclear Generation Ltd., Barnwood, Gloucester, GL4 3RS*

*<sup>e</sup>National Nuclear Laboratory, Sellafield, Cumbria, CA20 1PG*

*<sup>f</sup>School of Metallurgy & Materials, University of Birmingham, Birmingham, B15 2SE, UK.*

## Abstract

Herein, the first study is presented using 4D synchrotron X-ray microtomography to capture all stages of crack development in neutron irradiated and radiolytically oxidised nuclear graphite. Employing a novel loading setup, specimens of Gilsocarbon graphite, both unirradiated and irradiated at 301 °C to  $19.7 \times 10^{20}$  neutrons/cm<sup>2</sup> ( $\sim 2.6$  displacements/atom (*dpa*)), were loaded to generate a crack. All stages of the fracture process were then captured using synchrotron X-ray imaging. Reconstructed tomographic images and 3D segmented crack volumes have been used to observe and analyse the irradiation-induced evolution of the graphite microstructure as well as corresponding changes in the crack initiation, propagation, and arrest behaviour of graphite after neutron irradiation. Close examination of the applied stress-strain curves highlights the suppression of micro-crack-based damage accumulation in irradiated graphite. Moreover, as well as the crack-bridging and deflection mechanisms characteristic of unirradiated graphite, crack arrest in the irradiated graphite is shown to be significantly influenced by crack tip blunting. This change is associated with the growth of the open pore structure of graphite, specifically the enlargement and increased frequency of macro-pores, resulting from the simultaneous radiolytic oxidation of the graphite microstructure during neutron irradiation.

## 1. Introduction

Gilsocarbon is a synthetic, medium-grained nuclear graphite that has been used as a neutron moderator and structural support in reactors such as the experimental OECD HTR reactor DRAGON,

\* Corresponding author:

Tel: +44 (0)121 414 3959, E-mail: [j.m.wade@bham.ac.uk](mailto:j.m.wade@bham.ac.uk) (J. Wade-Zhu)

the German THTR and is the moderator in the UK's entire fleet of Advanced Gas-cooled Reactors (AGRs) that are still in operation today [1].

The microstructure of Gilsocarbon graphite is complex, consisting of spherical coke particles, or “filler” (typically 0.5-1 mm in diameter), surrounded by a carbonised coal-tar pitch binder phase, or “matrix”. Gilsocarbon also contains ~20% porosity in its unirradiated state. Around half of this is an open network of gas evolution and escape pores covering multiple scale-lengths (nm-to-mm), while the other half are closed pore features, specifically micro/nano-sized cracks that form due to the anisotropic contraction of crystallites during cooling after graphitisation at 2800-3000°C [2–4]. Such a large and varied flaw population is heterogeneously distributed throughout the microstructure of Gilsocarbon, causing its density to display significant spatial variability [5]. This translates into slightly anisotropic (near-isotropic) properties, substantial spread in property measurements, and significant specimen size effects [6–8]. As a result, characterising and understanding the structure-property-performance relationships of Gilsocarbon graphite has and continues to be a significant challenge.

X-ray computed tomography (XCT) has been shown to be a powerful tool for performing *in situ* observations of deformation and fracture processes in materials. In recent years, this technique has been used in multiple studies to provide an in-depth analysis of the different microstructural mechanisms that govern strength and fracture in unirradiated nuclear graphite [9–17]. These properties are of particular interest because of their direct relationship with component reliability and service lifetime. From these studies, larger pores and cracks within the graphite microstructure have been identified as local strain concentrators and key features from which crack initiation occurs [10,11]. In some instances, the development of stable micro-cracks has been shown to precede macro-crack initiation [13,14]. Continued crack development is characterised by the coalescence of cracks and their propagation to failure [10]. Pores/cracks within the graphite microstructure have also been shown to play an integral role in crack arrest mechanisms, in particular crack-bridging, crack deflection and micro-cracking ahead of the crack tip [9–12,14,16,17].

However, during service in a carbon dioxide-cooled nuclear reactor, such as an AGR, the microstructure of graphite is altered by two competing processes: neutron irradiation damage and radiolytic oxidation. Exposure to fast neutron irradiation causes the individual crystallites that make up graphite to expand in the direction of their stacking (*c*-axis) and contract normal to this direction (*a*-axis) [18]. The *c*-axis expansion of crystallites is accommodated for by the closure of basally-aligned pores and cracks, namely Mrozowski cracks [4,19], reducing the size and distribution of these features throughout the microstructure and increasing the graphite's overall density. Simultaneous to this, radiolytic oxidation internally corrodes the graphite, expanding and opening porosity networks and reducing the graphite's overall density [20,21]. These processes correlate with significant changes in the strength and fracture properties of nuclear graphite [22–28]. However, to date, there is a limited understanding of how the irradiation and radiolytic oxidation-induced evolution of the graphite

microstructure influences the microstructural mechanisms that govern the material's strength performance and fracture behaviour.

This article seeks to address this by presenting the results of the first time-resolved synchrotron X-ray microtomography (4D-XCT) experiments capturing multiple stages of fracture in unirradiated and irradiated Gilsocarbon (installed set graphite irradiated at 301 °C to  $19.7 \times 10^{20}$  n/cm<sup>2</sup> ( $\sim 2.6$  dpa)). Note, the use of “irradiated” throughout this manuscript is used for conciseness, but strictly refers to Gilsocarbon graphite that has been subjected to fast neutron irradiation and radiolytic oxidation. In the two specimens studied, observations of crack initiation, propagation and arrest are discussed in detail. Radiographs are used to elucidate the damage processes that precede macro-crack development and growth, while discernible differences in crack growth behaviour and toughening mechanisms are established from reconstructed tomographic images and 3D segmented crack volumes. Quantitative analysis of the graphite microstructure pre- and post-irradiation highlights an expansion of the largely open macro-pore network of graphite due to radiolytic oxidation. In conjunction with the atomic-scale damage sustained by the graphite during exposure to fast neutron irradiation, such changes to the microstructure are found to alter the nucleation and growth behaviour of cracks in this particular irradiated graphite, promoting significant improvements in strength and modifying toughening mechanisms.

## **2. Methods**

### **2.1 Materials**

The nuclear graphite grade used in this study was IM1-24 Gilsocarbon, a near-isotropic, polycrystalline graphite manufactured by AGL. Both the unirradiated and irradiated Gilsocarbon graphite used in this experiment was provided by EDF Energy Ltd (Barnwood, UK). The irradiated graphite specimen in this study was machined at Central Laboratory, National Nuclear Laboratory (Sellafield, UK) from graphite that had previously been part of an installed sample set from Hinkley Point B (HPB) reactor and then stored within the Windscale AGR graphite archive. At the time of removal in 1993, the reactor had reached a cumulative heat of 5676 GWd and the selected sets had a burn-up of  $\sim 59$  GWd/t at a temperature of 574 K. This was early in the life of HPB, thus the irradiated specimen in this work is considered to be representative of early-life reactor graphite. This is reflected in the relatively low neutron dose of the specimen, calculated at  $19.7 \times 10^{20}$  neutrons/cm<sup>2</sup> total (2.6 dpa), which is  $\sim 10$ -12% of its turnaround fluence ( $160$ - $200 \times 10^{20}$  neutrons/cm<sup>2</sup> (21-26 dpa) [29]), and the low weight loss, measured at  $\sim 4\%$ . Mass-volume densities of the unirradiated and irradiated specimens were measured as 1.845 g/cm<sup>3</sup> and 1.707 g/cm<sup>3</sup> respectively [30]. The initial density (prior to irradiation) of the irradiated specimen was 1.778 g/cm<sup>3</sup>. The difference in density of the unirradiated and pre-irradiated specimens is not deemed to be unusual and is associated with the natural variability

of Gilsocarbon, a result of the raw constituents and manufacturing processes used in its production [5]. It is worth noting that installed set graphite, although in this case identical in origin to moderator graphite, is not subject to the irradiation conditions in the reactor active core. However, given the low dose, low weight loss, early-life nature of the specimen in this particular study, irradiation-induced temperature differences in performance are believed to be small.

## 2.2 Sample Preparation

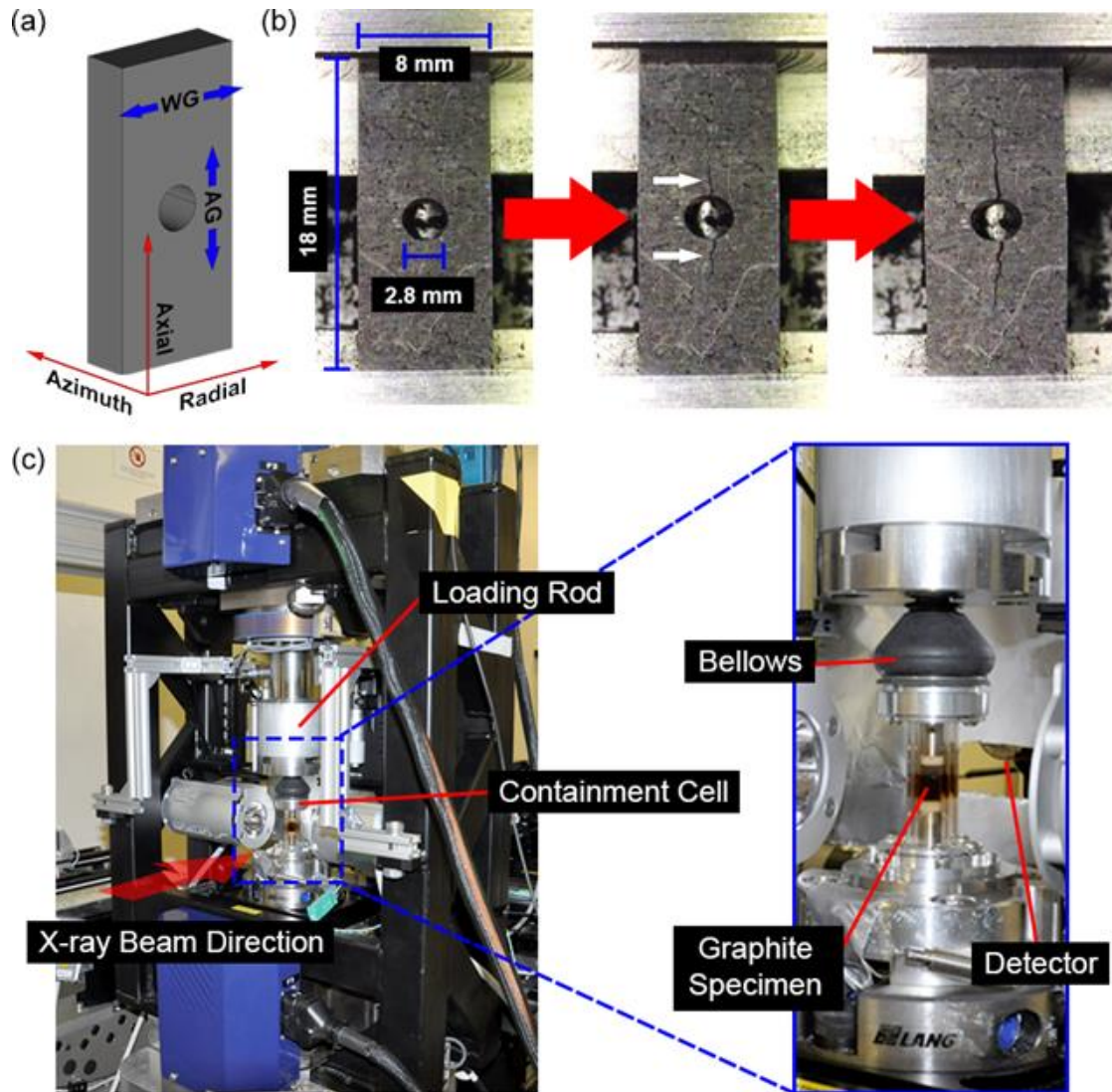


**Fig. 1:** Experimental setup used to examine stable crack growth in unirradiated and irradiated Gilsocarbon graphite using 4D synchrotron X-ray microtomography: (a) specimen geometry ( $18 \times 8 \times 3$  mm with a 2.8 mm hole) showing the orthogonal directions in which cuts were made with respect to the graphite billet and the WG = with grain and AG = against grain directions, (b) a demonstration of the cracks that form under compressive loading, (c) Deben 10kN load frame as setup on beamline I13 at Diamond Light Source with a close up of the double glass-walled containment cell.

The instability of crack growth in quasi-brittle systems like graphite under conventional fracture techniques presents a major challenge for X-ray tomographic microscopy studies as a finite time is required to obtain the images [31–33]. Therefore, a double cleavage drilled compression (DCDC) test geometry, based on the seminal work of Sammis and Ashby [34], in which a stable crack is formed and propagates under compressive applied loading with decreasing crack tip  $K_{IC}$  at increasing crack length, has been adopted for this study [35–37].

Unirradiated and irradiated Gilsocarbon graphites were machined into plates with  $l \times w \times d$  dimensions of  $18 \times 8 \times 3$  mm and a 2.8 mm hole at the centre. The anisotropic properties of Gilsocarbon (1:1.1 ratio as defined by the with and against grain coefficient of thermal expansion ratio in unirradiated graphite), caused by the preferential orientation of crystallite domains and aligned micro/nano-cracks perpendicular to the moulding/pressing (along the billets main axis) direction [38,39], means that the direction of machining requires careful consideration. In order to minimise potential mechanical performance differences resulting from bias within the graphite brick, all samples were machined such that the  $l \times w \times d$  of the plates equated to cuts in the graphite billet axial, radial and azimuth directions, see Fig. 1(a), the axial direction being the major axis of the original billet and also the direction of pressing during manufacture. Thus, subsequent loading of the specimens was performed parallel to the moulding/pressing direction. The final surface finish of the graphite specimens was kept as the as-machined surface for testing. The sequence of images in Fig. 1(b) show the compressive loading, highlighting the initiation of two single cracks at the top and bottom edges of the hole and stable propagation outwards from the hole towards the ends of the sample.

### 2.3 Mechanical Testing

Mechanical loading of the specimens was performed using a Deben 10 kN Open-Frame Rig (Deben UK Ltd, Suffolk, UK), see Fig. 1(c). In order to eliminate the risk of radiation contamination of the surrounding environment, irradiated graphite specimens were first sprung-loaded inside a double-glass-walled containment cell. To establish consistency between load measurements, the same procedure was also employed for unirradiated graphite specimens. Detailed descriptions of the loading rig and the containment cell are described elsewhere [40]. Considerable effort was made to ensure specimens were vertically-aligned with the direction of loading as well as about the rotational axis of the base stage in order to minimise precession during tomography scans. X-ray radiographs of specimens, captured at rotation angles of  $0^\circ$ ,  $90^\circ$ , and  $180^\circ$ , were used to confirm correct alignment. For each experiment, a uniaxial compressive load was applied to the specimen in accumulative steps by raising the lower stage of the open frame rig at a displacement rate of  $2 \mu\text{m}/\text{step}$ , during which the specimen was carefully monitored using a real-time load readout. A live X-ray radiograph video feed was used to identify cracking processes. These would appear as thin, irregular, bright lines in an otherwise dark background (refer to Fig. 11(a) and (c) for examples). The time between each step was

~15-20 seconds and was selected to account for any lag between an increase in applied load and the observable formation/extension of a crack. Under displacement control, the applied load on the specimen was increased until a crack formed in the graphite. The initiation of a crack was determined by small drops in applied load and confirmed by the live X-ray radiograph video feed. Once a crack had initiated, loading of the specimen ceased and a tomography scan was performed. Subsequent scans were completed on the crack after propagation under higher applied loads. Several tomography scans (three to five) were performed at intermittent points during crack propagation until the graphite specimen failed. Failure of the specimen was defined as the point at which crack growth became critically unstable, causing the specimen to rupture in a sudden and catastrophic manner. A quantitative manifestation of the event was a sharp and irrecoverable drop in the load-displacement curve. The applied stress in the graphite sample was calculated using eq. (1), the standard method for this test [34–37]:

$$\sigma = \frac{P}{BW} \quad (1)$$

where,  $P$  is the applied load,  $W$  is the sample width (8 mm) and  $B$  is the sample thickness (3 mm).

#### ***2.4 4D Synchrotron X-ray Microtomography***

4D XCT imaging of the unirradiated and irradiated graphite specimens was performed at the Diamond-Manchester Imaging Branchline I13-2 (DLS, Diamond Light Source, Didcot, UK) [41,42]. For each scan, the beamline's high-flux, partially-coherent, polychromatic 'pink' (30 keV) X-ray beam was used to acquire 4,001 projections, each of 200 ms exposure time, over a continuous rotation of 180° (fly scan). Prior to starting each experiment, a set of images were captured to account for fixed-pattern noise. These comprised of a set of flat-field images with the sample removed and a set of dark-field images with the beam off. Projections were collected using a PCO Edge 5.5 detector (PCO AG, Germany) coupled to a 500 µm CdWO<sub>4</sub> scintillator and a visual light microscope with 2.5× total magnification. The resultant field of view was 6.7 × 5.6 mm (2560 × 2160 pixels) with an effective pixel size of 2.6 µm. The limited field of view meant that the full length of the crack could only be captured on one side of the hole during the experiment, with the bottom side being selected throughout.

#### ***2.5 Data Analysis***

The raw radiographs of each scan were reconstructed with a filtered back projection algorithm incorporating ring artefact suppression [43,44]. The 32-bit images were converted to 8-bit and then imported into Avizo® 9.2.0 (FEI Visualisation Sciences Group, Mérégnac, France) for contrast

adjustment, post-processing and 3D rendering. In Avizo® 9.2.0, images were processed with a non-local means filter (applied in XY planes with a 42 px search window and 10 px local neighbourhood) and a bilinear filter (applied in 3D with a 7×7×7 px local neighbourhood) to reduce background noise. A Gaussian filter (applied in 3D with a 2×2×2 px local neighbourhood) was also employed to improve contrast between the pores/cracks and the graphite structure. Segmentation of the graphite volume was conducted using an image intensity threshold, the parameters of which were kept consistent across all datasets. The total porosity was determined by subtracting the graphite volume from the total volume. Avizo's "remove islands" wizard (applied in 3D) was then used to remove the closed pores from the total pore volume, leaving only the larger, interconnected open porosity networks. The closed pores were then segmented by selecting all the unsegmented regions of the volume. The highly porous microstructure of graphite meant that accurate segmentation of the cracks also required the removal of unwanted pores located along the crack path. This was accomplished by segmenting distinguishable parts of the crack in the image slices of each specimen and using Avizo's interpolation tool to segment parts where pores had obscured the crack. Crack face surface areas and crack volumes were determined using Avizo's quantification module and calculated based on the number of voxel faces/volumes that made up the segmented and smoothed 3D volumes of each crack captured by tomography. Crack opening displacements (COD) and crack lengths were measured in Fiji [45].

### **3. Experimental Results**

#### **3.1 – Microstructural Evolution**

High-resolution, reconstructed tomographic images presented in Fig. 2(a-b) show representative cross-sections of the unirradiated and irradiated Gilsocarbon graphite specimens prior to loading. In Fig. 2(a), the unirradiated graphite has a largely complete structure with only a small selection of singular, irregular-shaped pores visible (~0.15-0.3 mm in diameter) as well as some clusters of gas evolution pores, which appear to be predominately located within the binder matrix. A few lenticular-shaped cracks/pores are also observed. In Fig. 2(b), radiolytic oxidation of the graphite microstructure during exposure to fast neutron irradiation means there has been an expansion of the macro-scale pore structure (pores >10 µm in size). Individual pores have become larger in size and the total number of visible pores per unit volume has increased significantly, reducing the inter-pore spacing and increasing the interconnectivity of porosity networks.



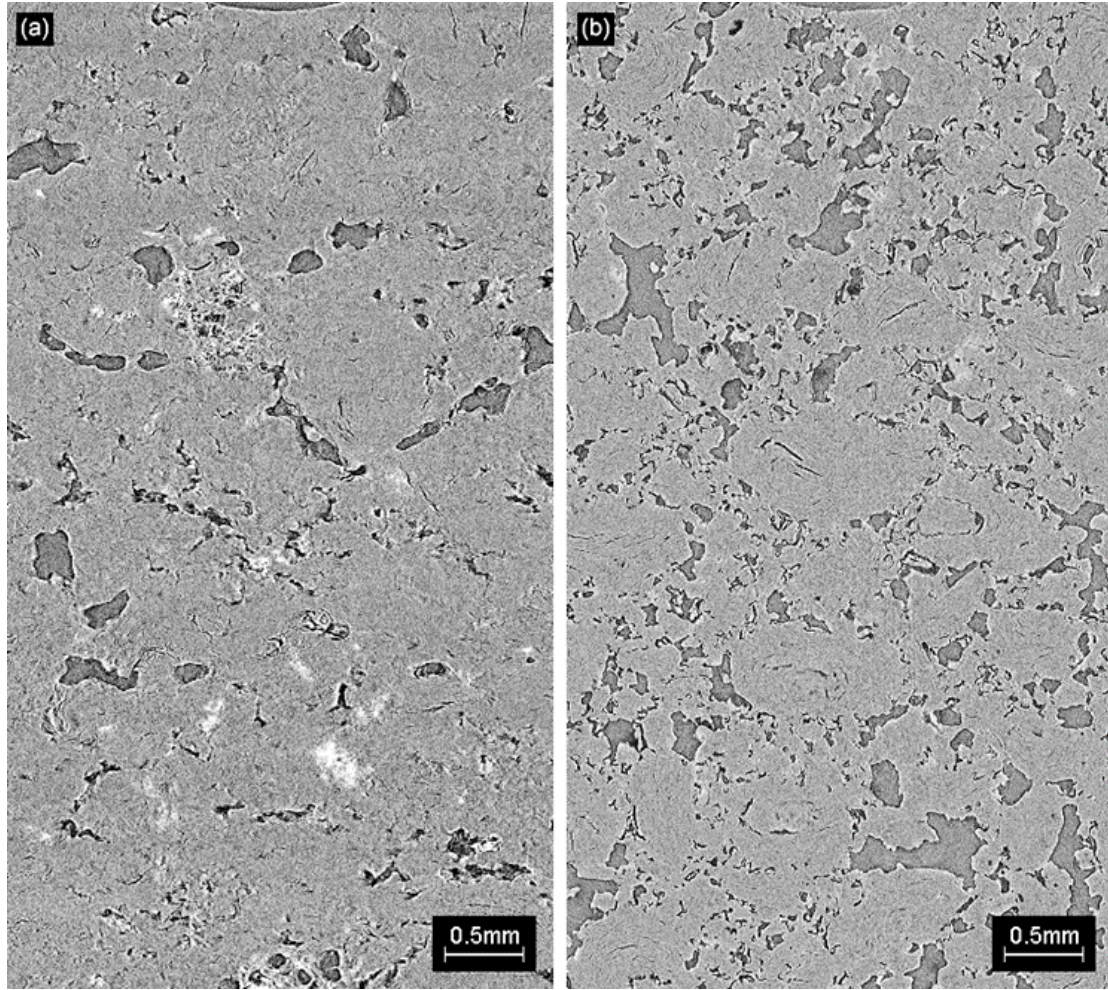


**Fig. 2:** Reconstructed tomographic cross-sectional images of the microstructures of the Gilsocarbon graphite prior to loading: (a) unirradiated, and (b) irradiated and radiolytically oxidised. Note, the lower edge of the hole in the middle of the specimen is located at the top of the images.

This is well-represented in the segmented 3D pore structures of the unirradiated and irradiated specimens shown in Fig. 3(a-f), where the amount of open porosity (dark blue volumes in Fig. 3b and e) has increased and the amount of closed porosity (light blue volumes in Fig. 3c and f) has decreased with irradiation. A quantitative analysis reveals an almost two-fold increase in the total pore volume between the unirradiated and irradiated Gilsocarbon specimens, a change in absolute volume from 6.39 mm<sup>3</sup> in the unirradiated graphite to 12.4 mm<sup>3</sup> in the irradiated. Separating this into open and closed porosity, comparatively, the irradiated specimen contains 2.6× more open porosity and 0.4× less closed porosity than the unirradiated specimen, with open porosity accounting for 67.5% of total porosity in the unirradiated Gilsocarbon and 89.6% in the irradiated. The aforementioned total increase in pore volume translates into a difference in graphite density between the unirradiated and irradiated specimens of 8.44%, a result that correlates well with the 7.77% difference in measured density between the two specimens.



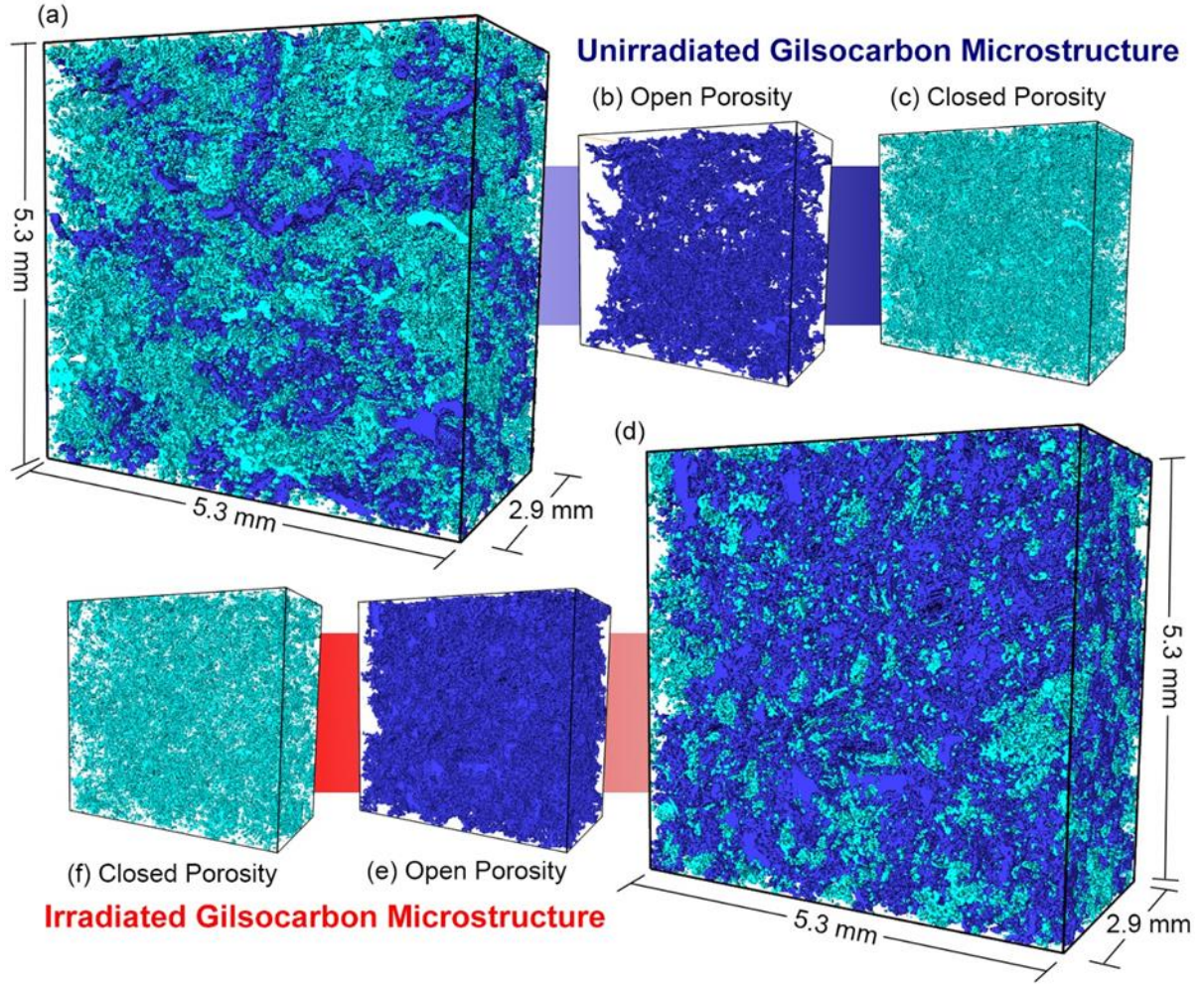


**Fig. 3:** 3D representation of the (a) unirradiated and (d) irradiated Gilsocarbon graphite microstructures together with individual 3D segmented volumes depicting irradiation-induced changes in (b and e) interconnected open porosity networks, and (c and f) closed porosity structures.

The size distributions of closed pores in both specimens are presented in the histogram in Fig. 4. A comparison of the results shows that, for the two specimens of this study, there is an almost 44% reduction in the peak frequency of closed pores in the irradiated Gilsocarbon. Moreover, there is no discernible shift to a larger size range. The latter would indicate that the closed pores in the irradiated graphite, and that fall within the resolution of these tomography scans ( $>2.6 \mu\text{m}$ ), are not part of the expanded pore structure and remain largely unaffected by the radiolytic oxidation that has taken place. This suggests that the reduction in their frequency may be explained by one or both of the following effects: (a) pre-existing differences in the amount of closed porosity in the unirradiated and pre-irradiated Gilsocarbon, directly related with the natural variability of the material; and/or (b) the expansion of open porosity following radiolytic oxidation leading to the penetration and eventual incorporation of closed pore structures into these open pore networks such that they are not included in

the analysis. In summary, while the change in overall density on radiolytic oxidation is small, the change in void size and shape distribution is significant.

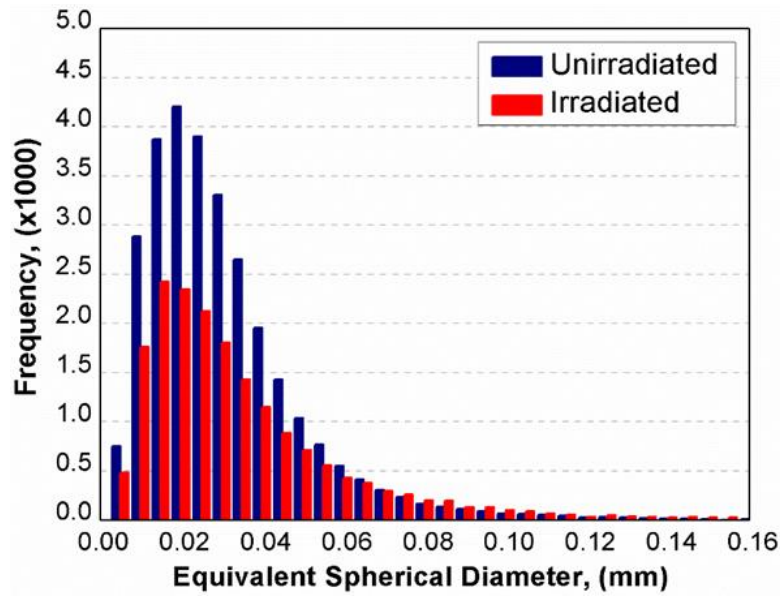


**Fig. 4:** Size distribution of closed porosity for the segmented volumes in Fig. 3(c) and (f).

### 3.2 – Loading Response and Fracture

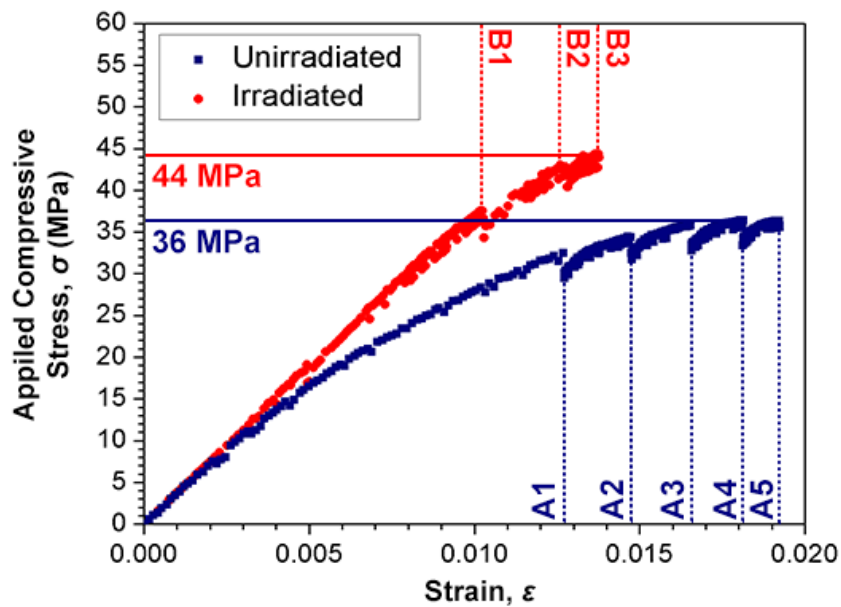


**Fig. 5:** Applied compressive stress-strain curves for the unirradiated (blue) and irradiated (red) Gilsocarbon. The dashed vertical lines indicate the points at which tomography scans were performed and correspond with the 3D segmented crack volumes in Fig. 6(a-b).

The compressive applied stress-strain curves generated during loading of the unirradiated and irradiated Gilsocarbon specimens are presented in Fig. 5. As shown, the unirradiated specimen displays a predominately non-linear loading response from zero load. This is typical of unirradiated Gilsocarbon graphite and has been demonstrated at multiple scale-lengths using a variety of conventional and micro-mechanical testing methodologies [9,33,46]. Generally referred to as “quasi-brittle” behaviour, it is associated with the activation of inelastic processes in the form of micro-cracking, even under very small loads [9]. *In situ* SEM observations of loaded specimens have demonstrated that stable micro-cracks are readily formed in unirradiated graphite [17,32,47]. By comparison, the irradiated graphite exhibits a much more linear stress-strain curve of higher gradient, the latter indicating that fewer non-recoverable processes have occurred. At a higher stress state, a non-linear loading response does begin to develop in the irradiated graphite, a likely indication of the eventual activation of micro-cracking. The dashed vertical lines in Fig. 5 highlight points during specimen loading at which tomography scans were performed. The decrease in stress at these points is associated with the relaxation of the specimens and load train under constant displacement following crack initiation/propagation, a process that occurs rapidly after an increase in applied load. Consequently, continued crack growth during tomography scans was negligible and had no discernible effect on the quality of the reconstructed tomographic images. The segmented 3D crack volumes that correspond with each of the tomography scans are presented in Fig. 6(a-b), together with corresponding measurements of average COD at the mouth of the cracks (CMOD) and average crack lengths. These capture three key stages of the fracture process: (i) crack nucleation/initiation, (ii) crack propagation, and (iii) critical failure of the specimen.



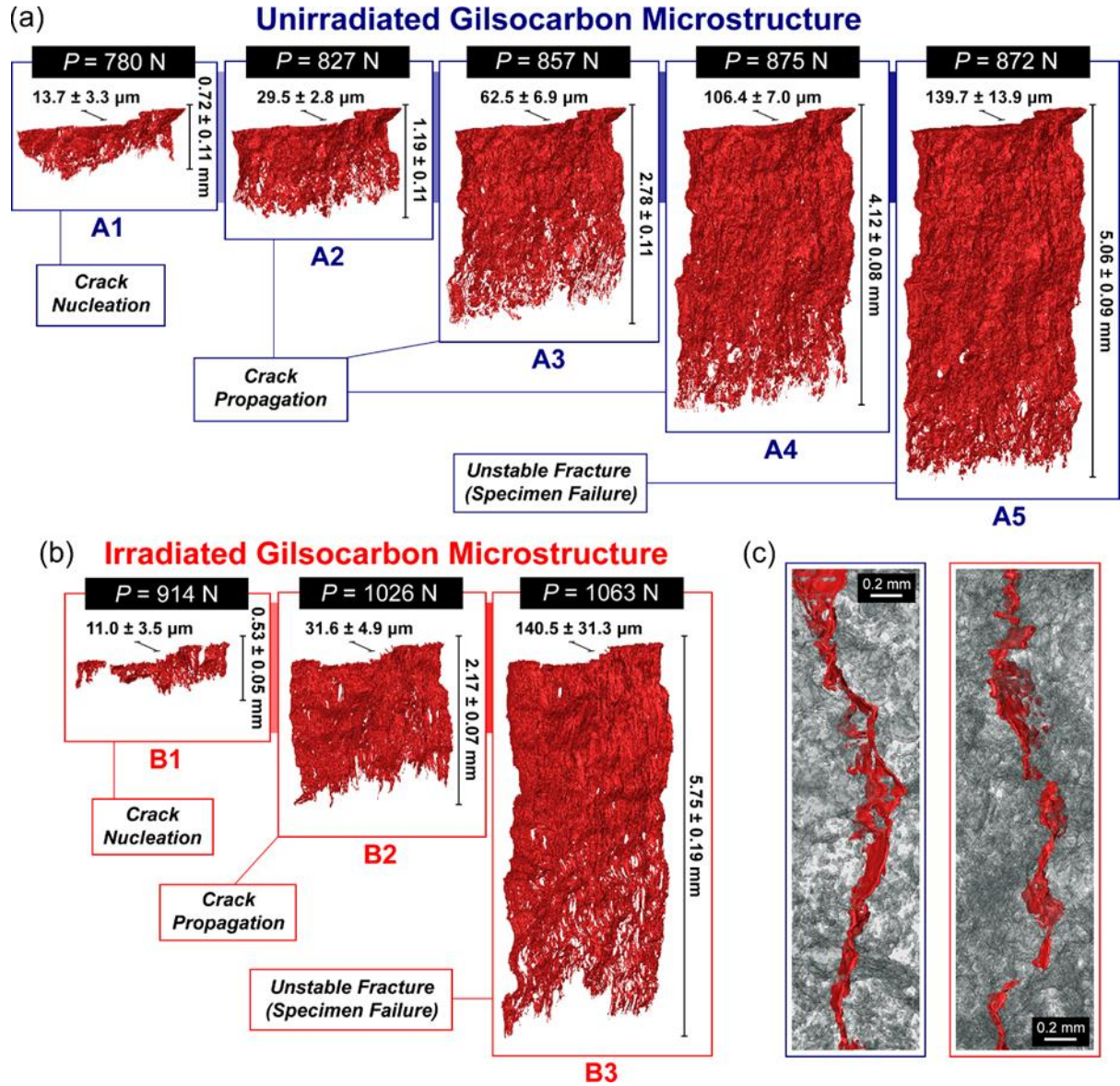


**Fig. 6:** Visualisation of 3D segmented crack volumes for each stage of loading ( $P$  = applied load) in (a) unirradiated Gilsocarbon, and (b) irradiated Gilsocarbon, with respective mean CMODs and average crack lengths. (c) presents a plan view of the cracks in A1 (blue border) and B1 (red border). Note, the width of all cracks is equivalent to the specimen width (3 mm).

As shown in Fig. 6(a), crack initiation in the unirradiated Gilsocarbon occurred at an applied stress of 32.5 MPa and a strain of 1.27%, generating a crack that was  $0.72 \pm 0.11$  mm in length, Fig. 6(a) A1. Further loading of the unirradiated specimen resulted in stable crack growth, the crack propagating vertically and away from the hole (normal to the generated tensile stress [10]). The relative ease with which crack growth could be controlled in the unirradiated graphite facilitated the capture of multiple stages of crack propagation at applied stresses of 34.46 MPa, 35.71 MPa and 36.46 MPa and crack lengths of  $1.19 \pm 0.11$  mm,  $2.78 \pm 0.11$  mm, and  $4.12 \pm 0.08$  mm respectively, Fig 6(a) A2-A4.

Failure of the specimen was achieved at an applied stress of 36 MPa and a strain of 1.92%. The length of the crack at this stage was  $5.06 \pm 0.09$  mm, Fig. 6(a) A5.

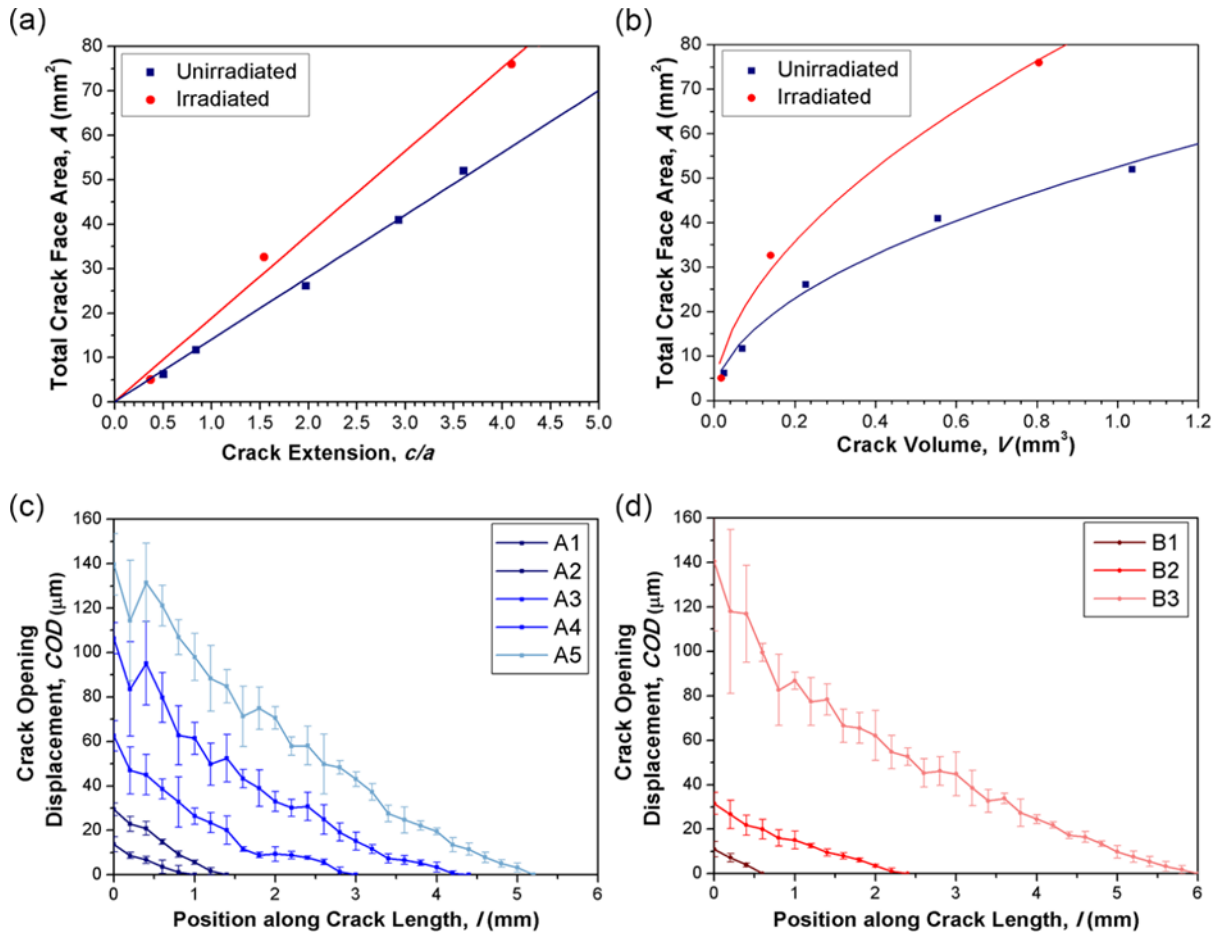


**Fig. 7:** Quantitative analysis of the segmented 3D crack volumes in Fig. 6(a-b): (a) total crack face area as a function of crack length, (b) total crack face area with respects to crack volume, (c) COD at sequential positions along the unirradiated crack length, and (d) COD at sequential positions along the irradiated crack length. The error bars in (c) and (d) show the standard deviation of each measurement.

Figure 6(b) shows that the first crack to develop in the irradiated Gilsocarbon was  $0.53 \pm 0.05$  mm in length and formed at an applied stress of 38.1 MPa and a strain of 1%, Fig. 6(b) B1. Beyond this, the crack growth behaviour was very different to that observed in the unirradiated specimen. Instead of progressive loading of the graphite translating into incremental increases in crack length, crack growth was effectively halted in the irradiated specimen until a significantly heightened stress state had been achieved. This is evidenced by the relatively large  $\Delta\sigma$  and  $\Delta\varepsilon$  between each tomography scan. Once the stress condition for crack propagation had been achieved, crack growth in the irradiated graphite ensued in both a sudden and unstable manner, ceasing precipitously at a length of  $2.17 \pm 0.07$  mm, Fig. 6(b)

B2. Similarly catastrophic behaviour has been reported by Heard *et al.* in radiolytically-oxidised PGA graphite up to 15% weight loss [47]. Failure of the irradiated specimen occurred shortly after at an applied stress of  $\sim 44$  MPa and a strain of 1.38%, Fig. 6(b) B3. Given that the crack lengths at failure were similar for the unirradiated and irradiated materials, this implies a significant increase in the failure strength (some 22% if one assumes the analysis in Sammis and Ashby to be valid [34]) and a decrease in strain-to-failure when compared with the unirradiated Gilsocarbon.

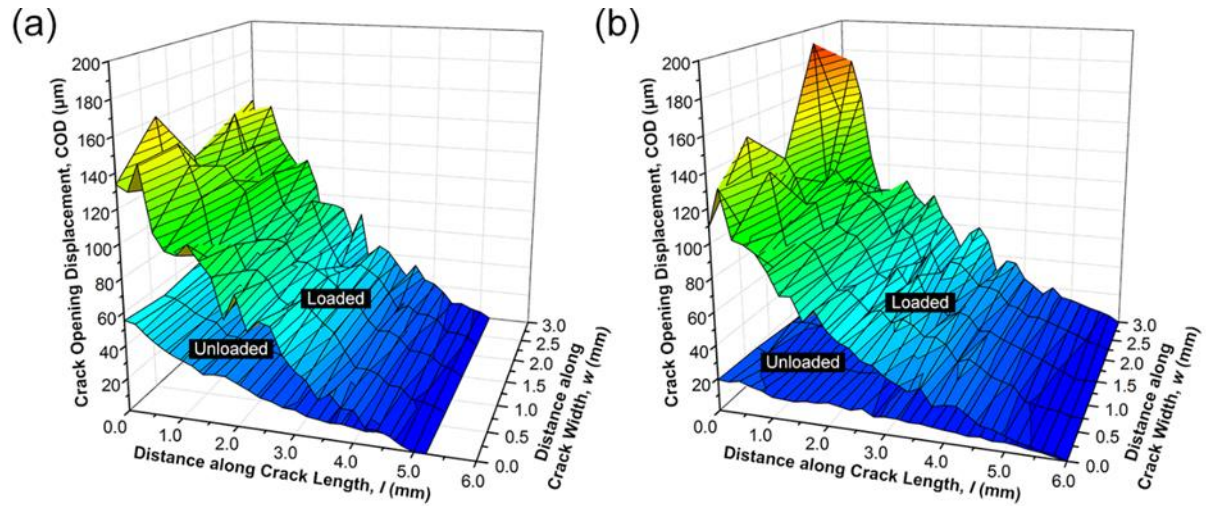


**Fig. 8:** 3D measurements of COD for cracks at peak load and after unloading in: (a) unirradiated, and (b) irradiated Gilsocarbon graphite.

A quantitative surface area analysis of the cracks generated in the Gilsocarbon specimens is presented in Fig. 7(a) and shows that both exhibit a linear increase with crack extension, the rate of this increase being higher in the irradiated graphite crack. Fig. 7(b) demonstrates that the larger surface area of the irradiated graphite crack does not correspond with a linear increase in crack volume. This would suggest that the irradiated crack has a more faceted geometry. COD measurements at sequential positions along the length of the cracks are presented in Fig. 7(c-d) and are an accumulation and average of COD values recorded over 10 different cross-sections of the cracks. Overall, the resultant trends are as to be expected, with the COD decreasing as measurements are made closer to the crack tip and larger maximal values of COD associated with cracks of longer length. A more detailed 3D analysis of COD comparing cracks in both the unirradiated and irradiated Gilsocarbon at peak load, A5 and B3 respectively, and after unloading is presented in Fig. 8(a-b). As shown, in both cases, COD measurements are relatively consistent across the width of the cracks. In establishing differences in the COD at the mouth of the crack (CMOD at  $l = 0$ ), the residual CMOD of the unloaded crack in unirradiated Gilsocarbon is 37.6% of that at peak load, meaning that 62.4% of deformation was recovered. This compares favourably with prior COD analysis completed by Barhli *et al.* using edge-

detection analysis and digital volume correlation (DVC), where the residual CMOD of an unloaded crack in unirradiated Gilsocarbon was ~30% of that at peak load [16]. In the irradiated Gilsocarbon in Fig. 8(b), the CMOD of the unloaded crack is only 12.4% of that a peak load, equating to 87.6% of deformation recovered. This result confirms that more of the deformation that has occurred in the unirradiated graphite specimen is permanent, with 40% less being recovered after unloading. As discussed below, this permanent deformation is associated with micro-cracking, a process that is shown to be restricted in the irradiated specimen.

### **3.3 – Crack Initiation**

In order to understand the effect microstructural changes in the Gilsocarbon due to neutron irradiation and radiolytic oxidation have on crack initiation, a comprehensive examination of the tomographic images was performed. Figure 8(a-h) and 9(a-h) are a representative view of crack initiation in the unirradiated and irradiated Gilsocarbon specimens, respectively. In both instances, cracks were found to nucleate predominately from larger open pore structures situated along the circumference of the hole. Lenticular cracks/pores were also identified as potential flaws from which cracks developed, see Fig. 9(b and f) and Fig. 10(a and e), but initiation from these features was dependent on their orientation ( $\sim 90^\circ \pm 30^\circ$ ) to the generated tensile stress. Instances of secondary cracking, whereby two individual cracks nucleate from the edge of the hole, were recorded in the unirradiated Gilsocarbon specimen, see Fig. 9(a and e), but these were highly-infrequent.

Noteworthy is that, even at this early stage in the fracture process, the crack in the unirradiated Gilsocarbon exhibits a number of kinks (points of high deflection). By comparison, the crack in the irradiated Gilsocarbon, despite propagating at various angles, follows a much straighter crack path morphology. This difference is perhaps best represented in Fig. 11(a-d), where radiographs, both raw and post-processed using an inverse filter and selective levelling to modify local contrast, provide a full “through-thickness” view of the cracks in both specimens. As shown in Figure 11(a-b), crack initiation in the unirradiated Gilsocarbon appears to occur at multiple through-thickness locations in a distributed region of high stress along the circumference of the hole, cracks of high tortuosity propagating along different crack paths before converging towards a single point. In Fig. 11(c-d), the crack in the irradiated Gilsocarbon initiates from a lone region along the circumference of the hole, the cracks generated being of equivalent tortuosity but following more linear crack paths.



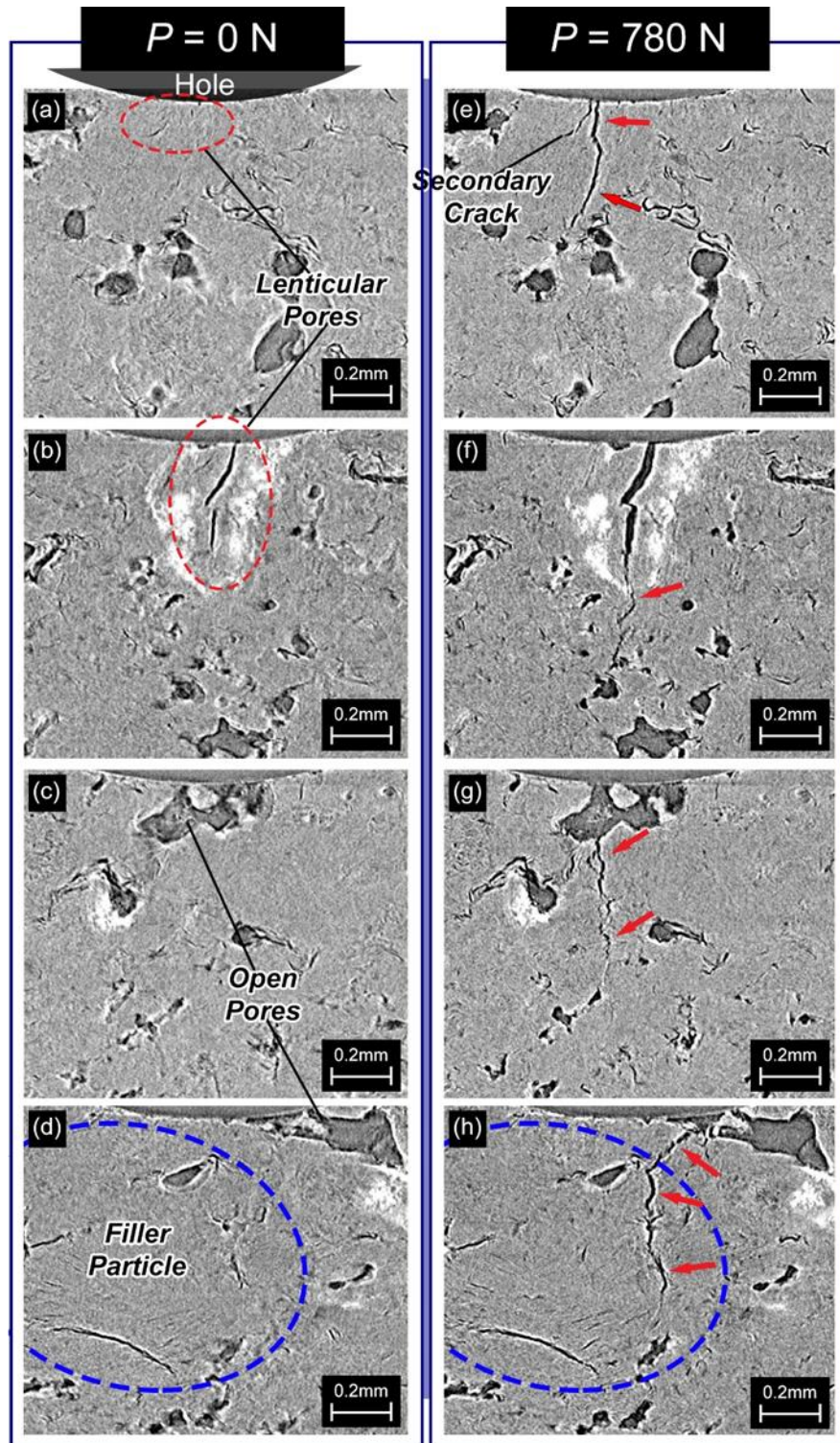


**Fig. 9:** Representative tomographic images of crack initiation from various microstructural features in unirradiated Gilsocarbon graphite: (a-d) microstructure prior to loading, and (e-h) microstructure after first crack develops (taken from crack A1 in Fig. 6(a)).

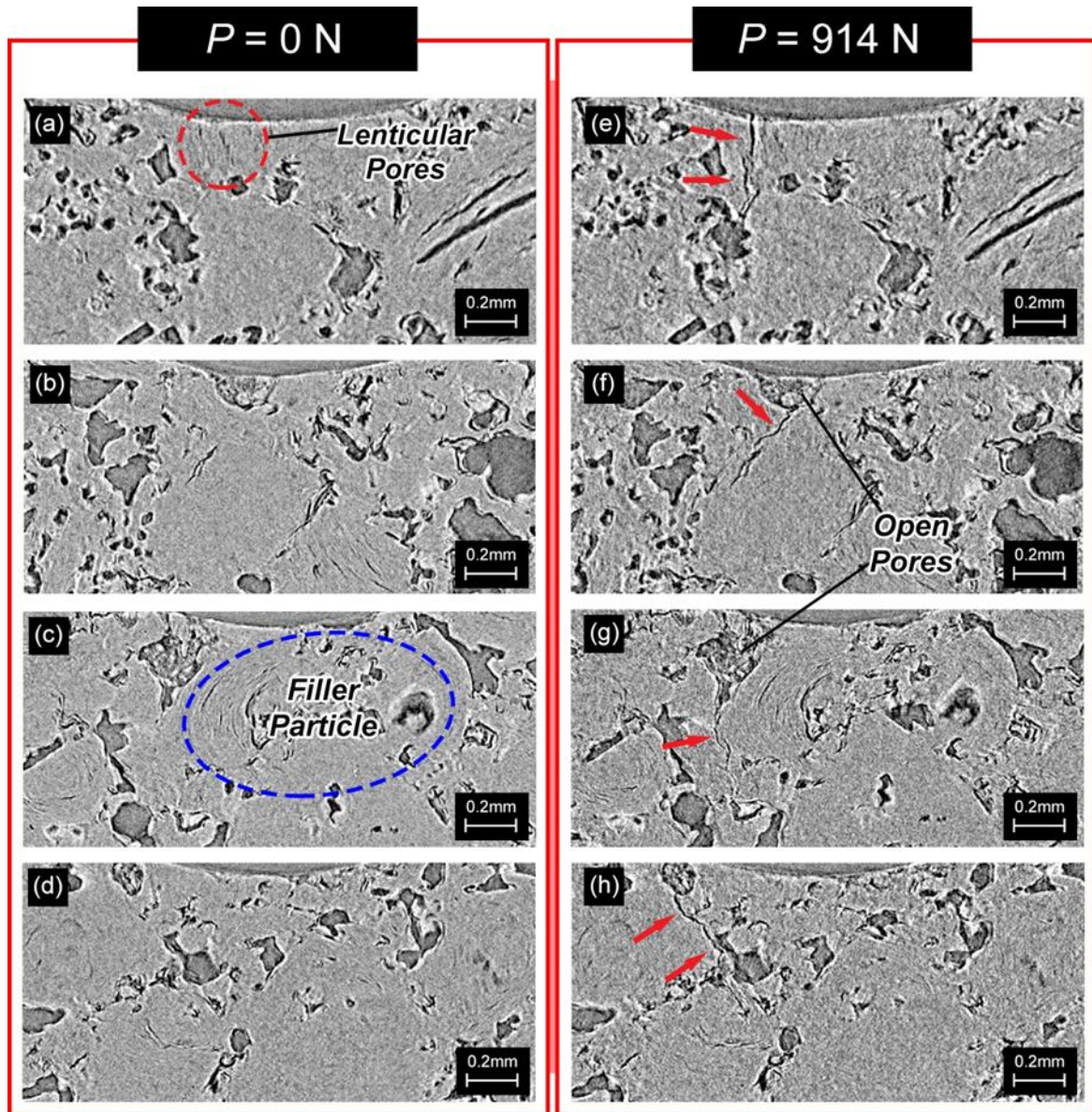


**Fig. 10:** Representative tomographic images of crack initiation from various microstructural features in irradiated Gilsocarbon graphite: (a-d) microstructure prior to loading, and (e-h) microstructure after first crack develops (taken from crack B1 in Fig. 6(b)).



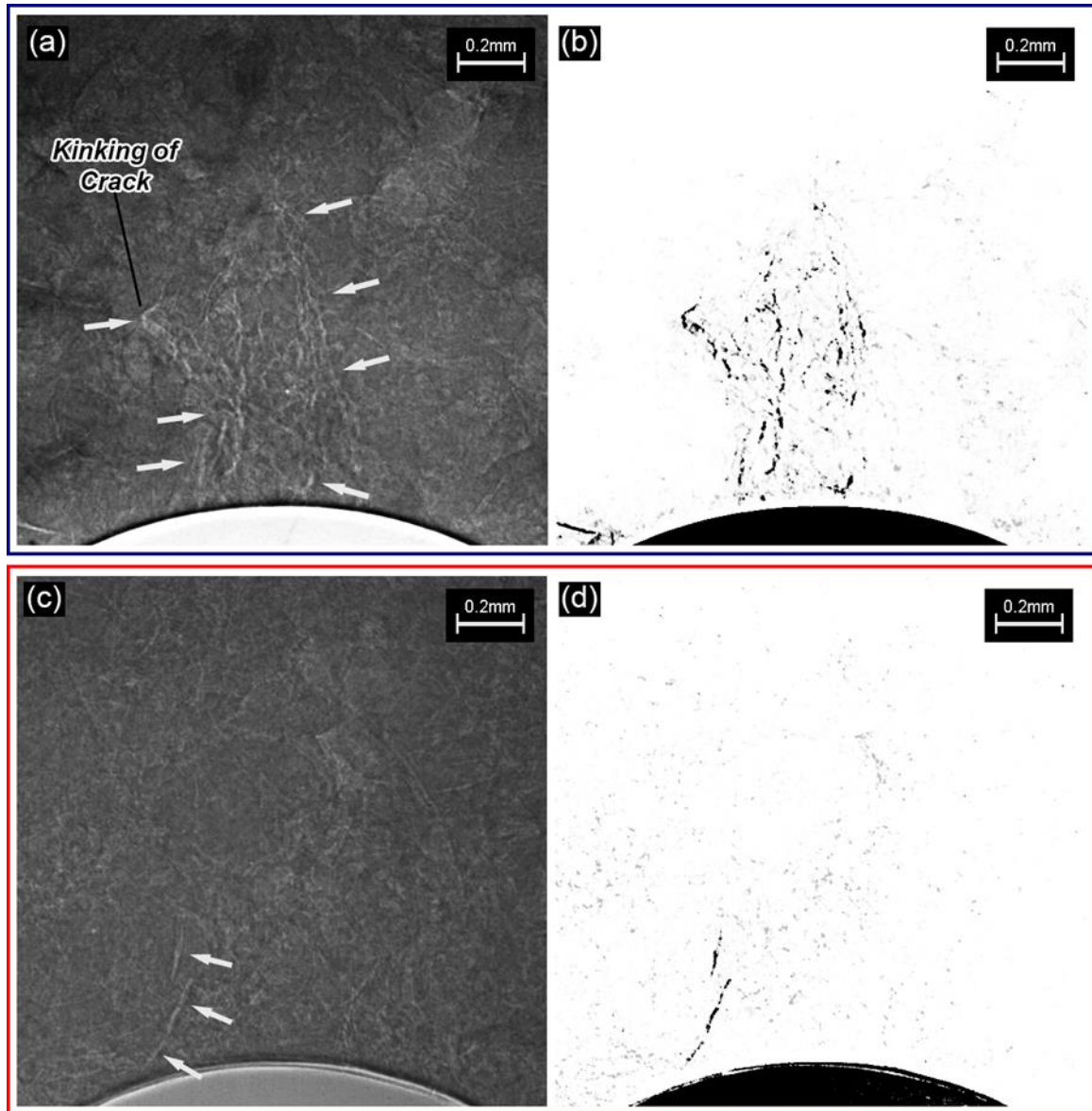


**Fig. 11:** Raw (a and c) and post-processed (b and d) radiographs capturing crack nucleation in: (a-b) unirradiated and (c-d) irradiated Gilsocarbon graphite. Notice the wide distribution of crack initiation sites across the circumference of the hole as well as the tortuous and kinked nature of the crack paths in the unirradiated Gilsocarbon specimen compared with the much narrower distribution and straighter cracks in the irradiated graphite specimen.

### 3.4 – Toughening Mechanisms

The principal benefit of using 4D-XCT to image deformation and fracture in Gilsocarbon graphite is it enables *in situ* observations of extremely complex crack geometries to be made across a 3D dataset and at different stages of crack growth. By closely examining the different interactions made between the crack and its surrounding microstructure as it propagates, insights on the microstructural

toughening mechanisms that evolve and are activated pre- and post-neutron irradiation and radiolytic oxidation can be formed.

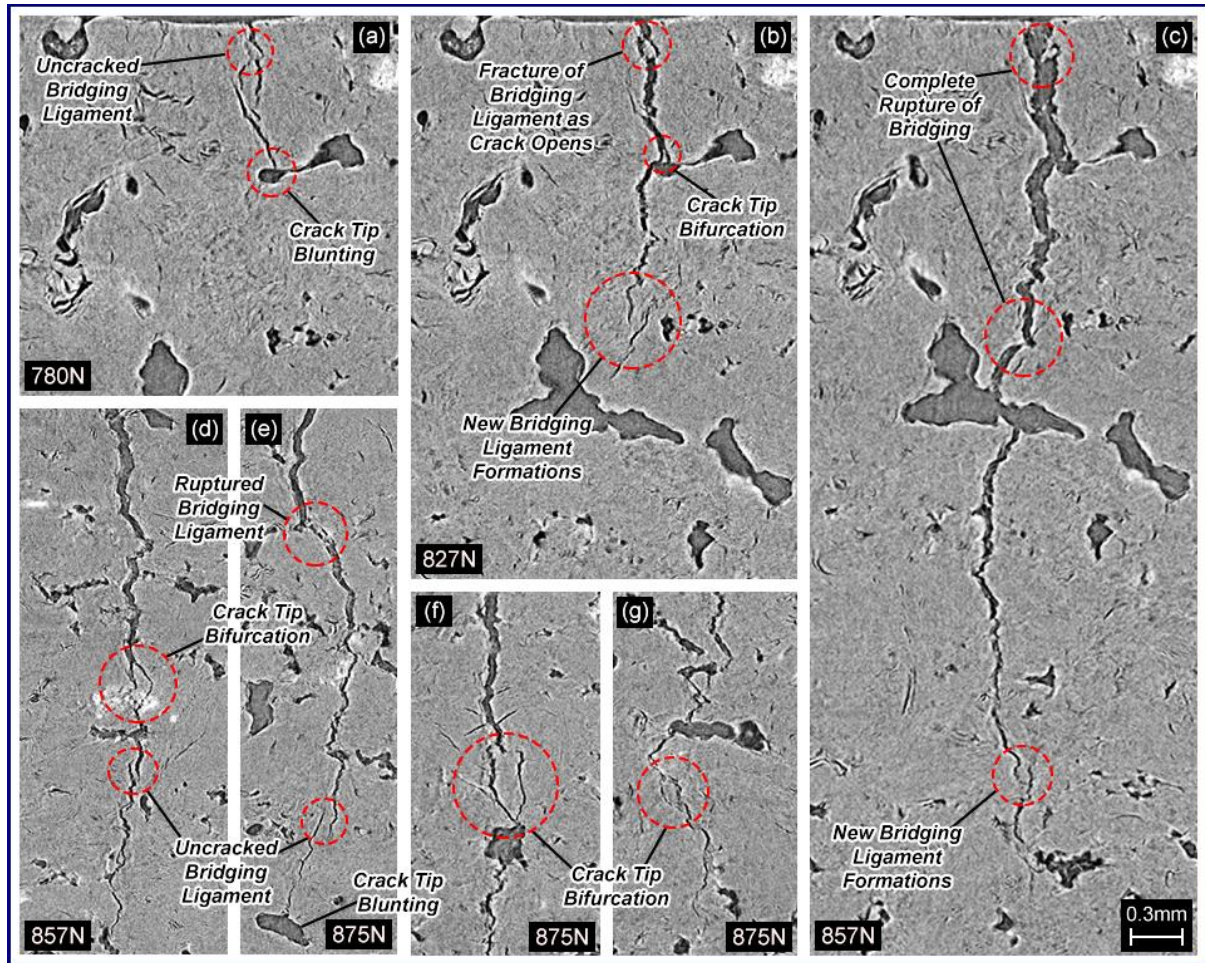


**Fig. 12:** Reconstructed tomographic images of the microstructural toughening mechanisms in unirradiated Gilsocarbon graphite. All images are cross-sections of the same crack captured at various stages of growth (see Fig. 6(a)). Each volume is made up of an individual stack of 1154 image slices. The relative through-thickness position at which images were taken of the crack can be determined based on the following slice numbers: (a-c) 1032, (d) 581, (e) 300, (f) 514, (g) 979, where 1 is the front image slice and 1154 is the back image slice. No filler particles could be identified in the images due to the closure of their characteristic lenticular pores under compressive loading.

As demonstrated in the reconstructed tomographic images in Fig. 12(a-g), the crack in the unirradiated graphite specimen is tortuous and contains numerous uncracked bridging ligaments. This highlights that both crack deflection and bridging are core toughening mechanisms in unirradiated Gilsocarbon, which is consistent with the literature [13,16,17,33,48]. Figures 12(a-c) provides a sequential overview of the crack-bridging process, showing an initial uncracked ligament in the wake



of the crack in Fig. 12(a), partial fracture of the same ligament as the COD increases in Fig. 12(b), and complete rupture of the ligament in Fig. 12(c). The same series of images also demonstrates the formation of new crack-bridging ligaments nearer the propagating crack tip. The prevalence of these two mechanisms across the entire crack volume is confirmed by the 3D segmented crack volumes in Fig. 6(a), where the persistent twists and kinks observed along the crack path and the convoluted topography of the crack surface is clear evidence of crack deflection. Meanwhile, distributed discontinuities in the crack volumes, particularly nearer the crack front, are associated with the connected ligaments between crack surfaces and are characteristic of crack-bridging [9]. Although crack deflection and bridging have been identified as major crack arrest mechanisms by which the rate of crack growth was slowed in the unirradiated graphite specimen, Fig. 12(d-g) also highlights the occurrence of minor toughening mechanisms in the form of crack tip bifurcation and crack tip blunting.

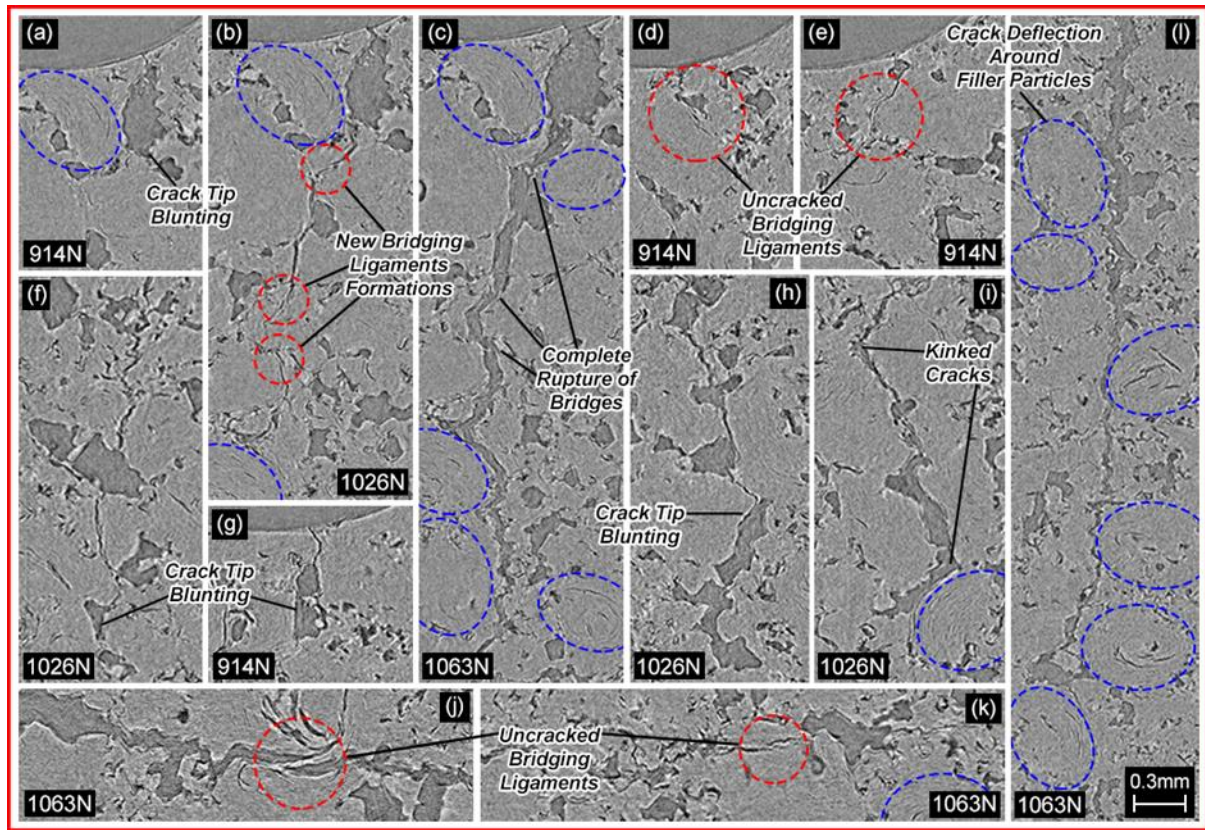


**Fig. 13:** Reconstructed tomographic images of the microstructural toughening mechanisms in irradiated Gilsocarbon graphite. All images are cross-sections of the same crack captured at various stages of growth (see Fig. 6(b)). Each volume is made up of an individual stack of 1154 image slices. The relative through-thickness position at which images were taken of the crack can be determined based on the following slice numbers: (a-c) 259, (d) 778, (e) 343, (f) 502, (g) 932, (h) 806, (i) 684, (j) 643, (k) 830, (l) 574, where 1 is the front image slice and 1154 is the back image slice. Filler particles that are identifiable in the images are marked with a blue ring.

In the irradiated Gilsocarbon, crack growth would appear to occur along the filler-binder boundary. This is well-demonstrated in Fig. 13(a-c) and again in Fig. 13(l), where the progressive stages of growth are shown with the propagating crack front deviating around highlighted fillers either side of the crack. Please note, only features clearly identifiable as filler particles are circled and it is likely there are more filler particles present either side of the crack than is depicted. The sharp deviations in the propagating crack path and the multiple crack-bridging ligaments visible in Fig. 13(a-l) reveal that crack deflection and bridging remain core toughening mechanisms. This is confirmed by the 3D segmented crack volumes in Fig. 6(b). No incidences of crack tip bifurcation were recorded in the irradiated graphite specimen. However, as demonstrated in many of the images in Fig. 13(a-l), crack tip blunting, characterised by the crack tip entering a pore without exiting out the other side, was widespread and identified at every stage of crack growth.

## 4. Discussion

### 4.1 Crack Initiation

XCT imaging has enabled direct observations of crack initiation in unirradiated Gilsocarbon graphite and that irradiated at 301 °C to  $19.7 \times 10^{20}$  neutrons/cm<sup>2</sup> and radiolytically oxidised to 4% weight loss. Figure 11(a) shows that cracks in the unirradiated specimen nucleate from numerous crack initiation sites and follow a number of differing crack paths. A plan view of the macro-crack produced after initiation in Fig. 6(c) also shows that it is formed of several distinguishable sections, each with their own vertical and lateral angles of propagation. The seemingly fragmented nature of the initial crack in Fig. 6(c) combined with the findings in Fig. 11(a) would suggest that crack initiation in the unirradiated graphite specimen is a chaotic process that evolves as multiple incidences of local fracture from flaws subject to high strain concentrations [10,11,14], specifically large irregular- and lenticular-shaped cracks, as shown in Fig. 9(a-h). These individual cracks then join together via lateral crack propagation that occurs simultaneous to vertical (axial) crack propagation, eventually merging into the single macro-crack captured in Fig. 6(a) A1. The kinks in the crack shown in Fig. 6(c) can be explained by instances of severe misorientation between nucleating cracks, causing them to join at sharp angles. The above hypothesis is consistent with the observation that the highly-heterogeneous microstructure of graphite causes load transfer under deformation to be non-uniform and affected by local changes in modulus [49]. As a result, the distribution of strain in graphite has been proven to be discontinuous and capable of developing in high concentrations at multiple separate locations [10,11,14,49], each of which can be considered potential sources for crack nucleation. In the irradiated Gilsocarbon specimen studied, Fig. 11(b) reveals that, whilst crack initiation occurs from the same flaw structures as those in the unirradiated graphite specimen, see Fig. 10(a-h), the higher statistical prevalence of these features following radiolytic oxidation leads to a narrower distribution of crack nucleation sites, an indication

of a more cohesive crack initiation process. However, as is also shown in Fig. 10(a-h), nucleated cracks in the irradiated Gilsocarbon specimen extend in a variety of different directions. This supports crack initiation in the irradiated graphite occurring as discrete local fracture and coalescence in the formation of a single macro-crack. A plan view of the crack in Fig. 6(c) also supports this, displaying gaps between the individual sections of the crack, again, each with their own vertical and lateral angles of propagation. The similarities displayed by both specimens leads to the conclusion that, at the scale-lengths at which XCT is able to operate, there is no identifiable change in the crack initiation behaviour of the Gilsocarbon specimens characterised in this study. This is consistent with the higher strength of irradiated graphites being generally attributed to irradiation-induced increases in elastic modulus (see Fig. 5) caused by the introduction of crystalline residual strains and the pinning of dislocations at the atomic-scale [25,50] rather than any sort of mechanistic change in crack initiation at the macro-scale. This study provides a direct experimental observation of this for the first time.

#### *4.2 Crack Propagation and Arrest*

Based on the 3D segmented crack volumes in Fig. 6(a-b) and the reconstructed tomographic images in Fig. 12(a-g) and 13(a-l), crack deflection, crack-bridging, and crack tip blunting have been identified as active mechanisms by which crack growth rates are regulated in both the unirradiated and irradiated Gilsocarbon specimens. The non-linearity of the stress-strain curves in Fig. 5 and the incomplete elastic recovery displayed in Fig. 8(a-b) also provides indirect evidence of micro-crack shielding in both graphites. However, despite having the same active mechanisms, detailed analysis of the 3D datasets captured at multiple stages of crack growth using 4D-XCT reveals distinct differences in the extent to which each contributes to crack arrest in the unirradiated and irradiated Gilsocarbon specimens. These differences are shown to be microstructurally-driven and are found to have a profound impact on the crack propagation behaviour (see description given in section 3.2).

Micro-crack shielding, for example, requires the generation of micro-cracks in a ‘fracture process zone’ ahead of microstructural flaws and/or crack tips [17,33], toughening graphite by releasing built-up strain around these features, thereby shielding them from far-field stresses [32], and using energy that would otherwise be available for macro-crack extension. However, given the linearity of the stress-strain curve in Fig. 5, it may be inferred that fewer micro-cracks have formed in the irradiated Gilsocarbon during specimen loading. This is further confirmed by the 3D-COD analysis presented in Fig. 8(a-b), where the recovery of more elastic deformation in the unloaded crack in the irradiated Gilsocarbon indicates less permanent, non-recoverable damage in the form of micro-cracks. The suppression of micro-cracking in the irradiated Gilsocarbon is associated with the elimination of flaws from which they can develop. Irradiating graphite is known to close micro-to-nano-sized cracks as they accommodate the net expansion of graphite crystallites [51,52]. This reduction in both the number and size of these flaws on irradiation lowers the probability of their contribution to crack growth processes

when compared to unirradiated graphite. Consequently, with fewer micro-cracks developing during specimen loading, micro-crack shielding will make a smaller contribution to toughening in the irradiated Gilsocarbon.

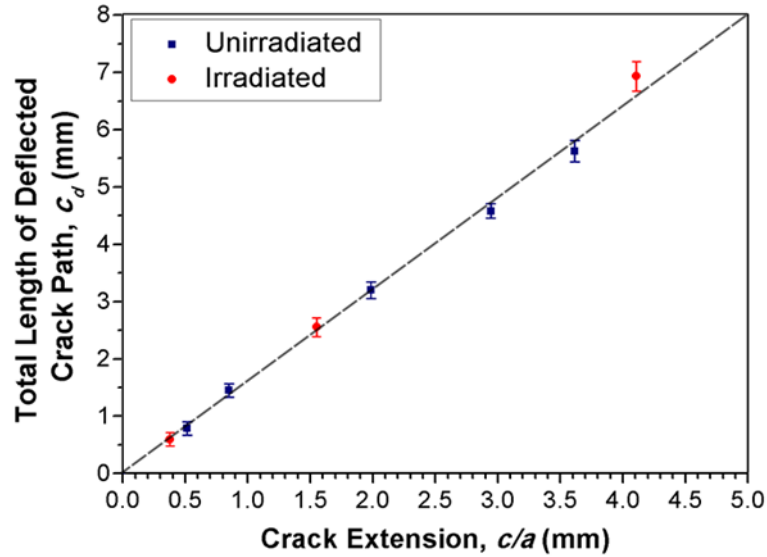


**Fig. 14:** The accumulative length of the deflected crack paths generated in both unirradiated and irradiated Gilsocarbon as a function of crack extension.

In terms of crack deflection, the morphology of the 3D segmented crack volumes in Fig. 6(a-b) confirm that cracks in both the unirradiated and irradiated Gilsocarbon specimens studied extend along deflected paths. This is perhaps to be expected as crack deflection in graphite is predominately governed by the distribution of filler particles throughout the graphite matrix [10,15] and the continued existence of a weak filler-binder interface [10,32]. As illustrated in Fig. 13(l), the former is largely unaffected by neutron irradiation and radiolytic oxidation. This has been observed to much higher weight losses in both thermally and radiolytically-oxidised nuclear graphite [15,53,54]. Meanwhile, the latter is only amplified by the irradiation-induced “hardening”, which both strengthens and stiffens the filler particles of the graphite, and preferential radiolytic oxidation of the binder phase [54], that simultaneously weakens the graphite matrix (*irrad<sub>particle</sub>*  $\sigma = 652$  MPa,  $E = 37.5$  GPa vs. *irrad<sub>matrix</sub>*  $\sigma = 357$  MPa,  $E = 8.6$  GPa [46]). There is quantitative evidence in Fig. 7(a-b) which suggests that the crack in the irradiated Gilsocarbon specimen is ~35% more deflected than that in the unirradiated specimen. However, as presented in Fig. 14, measurements of the total length of the entire deflected crack path (an accumulative measurement of all parts of the crack) as a function of crack extension (a straight-line measurement from crack opening to crack tip), made using Fiji image analysis software, shows no appreciable differences. This is in agreement with the findings of Hodgkins *et al.* [10], where cracks in unirradiated and radiolytically oxidised graphite up to 44% weight loss were found to be of largely



comparable morphology. Thus, it is probable that the higher crack face area of the crack in the irradiated Gilsocarbon is caused by events that occur at a smaller (micro) scale-lengths, e.g. the creation of an etched graphite surface texture following radiolytic oxidation, which has been demonstrated elsewhere [46,55,56].

Discontinuities in the 3D segmented crack volumes in Fig. 6(a-b) highlights the presence of crack-bridging in both the unirradiated and irradiated Gilsocarbon specimens. Clear examples of the mechanism are shown in Fig. 12(a-e) and 13(a-e, j and k). There was no measurable difference in the frequency of uncracked bridging ligaments (typically 2-3 located nearer the crack front), their breadth (~15-30  $\mu\text{m}$ ), nor the depth with which they are located in the wake of the crack in either graphite specimen. This would suggest that, in this particular instance, the process and its contribution to crack arrest remains largely unchanged with irradiation. Crack-bridging relies on the presence of voids and defects throughout the graphite microstructure and their ability to change the direction of the crack path such that the crack propagates around solid features to create bridging ligaments [17]. As mentioned previously, irradiation and radiolytic oxidation eliminates some of the smallest pores/cracks and expands the largest, respectively. The limited affect this has on crack-bridging indicates that either the irradiation-induced changes to the microstructure in the low dose specimens in this study are insufficient to influence the crack-bridging mechanism, and/or the defect size range that is altered by irradiation and radiolytic oxidation is outside the scale-length relevant to crack-bridging.

The most noticeable difference between the unirradiated and irradiated Gilsocarbon is the increased incidence of crack-tip blunting, see Fig. 13(a, f, g, and h). This appears to be the primary means by which uncontrolled crack growth is impeded in the irradiated specimen studied, especially given the reduced contribution of micro-crack shielding. This process involves a crack entering a pore such that the crack tip radius increases, modifying the stress intensity factor,  $K_I$ , so that a higher applied stress is required for further crack propagation. In accordance with the model of Deng *et al.* [57], crack tip blunting in the irradiated Gilsocarbon (pore sizes = ~200-400  $\mu\text{m}$  in diameter) should yield reductions in  $K_I$  at the crack tip of ~5-10%. This is in the range of expected changes in fracture toughness with irradiation alone [23,27,28]. The existence of crack tip blunting in the irradiated Gilsocarbon sample is relatable to the increased open pore structure following radiolytic oxidation, the higher density of larger macro-pores throughout the microstructure in Fig. 2(b) increasing the probability of crack-pore interactions. This is shown by, on average, >60% of the propagating crack front in the irradiated Gilsocarbon specimen being covered with pores, compared with <35% for the crack in the unirradiated specimen. The emergence of crack tip blunting as a significant toughening mechanism in the irradiated Gilsocarbon specimen is consistent with the description of fracture given in section 3.2. The sporadic manner in which crack growth ensues in the irradiated graphite specimen can be associated with instantaneous changes in crack tip radius (which is assumed to be near-zero for an ideal crack front) as it enters and exits pores of differing size. Moreover, the instability of crack growth after exiting a pore can be linked to the rapid release of high amounts of elastic strain energy that is stored in the irradiated

graphite, a product of the material's increased fracture strength and the high stress states required to overcome blunted crack tips. By comparison, in unirradiated Gilsocarbon specimen studied, the greater propensity for micro-cracking in regions where stress concentrations are high enables the controlled release of elastic strain energy. Consequently, the elastic strain energy stored in the material is never substantial enough to cause the same abrupt crack growth observed in the irradiated graphite specimen [10,14]. As shown in Fig. 13(h and i), this instability is further promoted by the fact that the increased size and frequency of pores in the microstructure, whilst being the dominant contributor to crack arrest by facilitating crack tip blunting under the appropriate conditions (e.g. an adequate coverage of pores along the crack front), also provide an alternative, resistance-free route for crack growth. This likely explains why, despite exclusive exposure to fast neutron irradiation having a toughening effect on graphite as a function of irradiation dose [23,26,27], its combination with radiolytic oxidation reverses this trend to produce a net reduction in fracture toughness that is only magnified with increasing irradiation dose and weight loss [28].

## 5. Conclusions

For the first time, 4D synchrotron X-ray computed microtomography has been used to capture crack initiation, propagation, and arrest in neutron irradiated and radiolytically-oxidised nuclear graphite. The main conclusions of this paper are as follows:

- Crack growth is shown to proceed in the unirradiated Gilsocarbon specimen in a steady and controlled manner. However, in the irradiated Gilsocarbon specimen (irradiated at 301 °C to  $19.7 \times 10^{20} \text{ n/cm}^2$  ( $\sim 2.6 \text{ dpa}$ )), this transitions into an abrupt and unstable process. This change in behaviour is linked with the evolution of the graphite microstructure following exposure to fast neutron irradiation and radiolytic oxidation.
- Crack initiation is found to follow the same mechanism in both unirradiated and irradiated Gilsocarbon specimens, namely by incidences of discrete local fracture in which individual cracks nucleate from irregular-shaped macro-pores as well as lenticular cracks and join together via lateral crack propagation to form a single macro-crack.
- The extent to which various toughening mechanisms contribute to the crack growth rate of unirradiated and irradiated Gilsocarbon has been investigated and it is shown that, for the specimens studied, crack deflection and crack-bridging are unaffected by irradiation and radiolytic oxidation.

- The irradiation-induced closure of micro-to-nano-sized cracks and pores is associated with the suppression of micro-cracking ahead of complex microstructural features and/or crack tips in the irradiated Gilsocarbon specimen.
- The expansion and increased frequency of macro-pores in the microstructure of the irradiated Gilsocarbon specimen leads to the emergence of crack tip blunting as a dominant toughening mechanism. This, combined with the suppression of micro-cracking, is believed to be the primary cause for the change in crack propagation/arrest behaviour in the irradiated graphite specimen of this particular study.

The limited literature available on fracture in neutron irradiated and radiolytically oxidised nuclear graphite means that many of the above findings are novel and provide potential new insights into the behaviour of in-reactor graphite. The prospective impact of this on the wider nuclear graphite community is two-fold. Firstly, an improved understanding of how microstructural features influence the macro-properties and in-service behaviour of irradiated graphite enables graphite manufacturers to develop superior graphite grades with optimised microstructures that maximise performance. Secondly, the fracture analysis presented above assists computational modelling that links the structure, properties and performance of nuclear graphite [58]. These models are used to predict the lifetimes of graphite-moderated reactor cores and, thus, play a vital role in ensuring their safe operation.

## Acknowledgments

The authors gratefully acknowledge the financial support from Innovate UK (IUK) under grant TS/M007723/1, “*Influence of Creep and Geometry on Strength of Irradiated Graphite Components*”. PMM thanks the Office for Nuclear Regulation for funding his post. The authors also acknowledge the services of NNL in machining the highly oxidised and irradiated graphite specimens necessary for this study. Firstly, the authors must thank the team at the University of Manchester, William Bodel, Joshua Taylor, and Matthew Roy, for their help in the preparation and running the experiment. The authors also thank Diamond Light Source and the team at beamline I13-2 (proposal MT16668), specifically Shashidhara Marathe, David E. Eastwood and Kaz Wanelik, for their help and cooperation in facilitating such challenging experiments. The authors also thank Prof P.J. Withers and Dr. Tristan Lowe and acknowledge the support from the Henry Moseley X-ray Imaging Facility (MXIF) at the University of Manchester. We also thank the many members of staff who have helped to make this research possible; Alan Steer, Jonathan Wright, and Simon Fox from EDF Energy Generation, Jon Bradley from NNL, Ed Williamson-Brown from Deben UK and many others for their helpful advice, comments and discussions. The views expressed in this paper are those of the authors and do not necessarily represent their organisations.

## References

- [1] B.J. Marsden, G.N. Hall, Graphite in gas-cooled reactors, 2012. <https://doi.org/10.1016/B978-0-08-056033-5.00092-6>.
- [2] A.L. Sutton, V.C. Howard, The role of porosity in the accommodation of thermal expansion in graphite, *J. Nucl. Mater.* 7 (1962) 58–71. [https://doi.org/10.1016/0022-3115\(62\)90194-0](https://doi.org/10.1016/0022-3115(62)90194-0).
- [3] P.J. Hacker, G.B. Neighbour, B. McEnaney, The coefficient of thermal expansion of nuclear graphite with increasing thermal oxidation, *J. Phys. D. Appl. Phys.* 33 (2000) 991–998. <https://doi.org/10.1088/0022-3727/33/8/316>.
- [4] S. Mrozowski, Mechanical strength, thermal expansion and structure of cokes and carbons, *Proc. 1st 2nd Conf. Carbon.* (1956) 31. <https://doi.org/papers://D9F9AA35-5CC8-482E-89C5-625C9FC6984D/Paper/p2585>.
- [5] J.D. Arregui-Mena, W. Bodel, R.N. Worth, L. Margetts, P.M. Mummery, Spatial variability in the mechanical properties of Gilsocarbon, *Carbon.* 110 (2016) 497–517. <https://doi.org/10.1016/j.carbon.2016.09.051>.
- [6] M. Sakai, H. Kurita, Size-Effect on the Fracture Toughness and the R -Curve of Carbon Materials, *J. Am. Ceram. Soc.* 79 (1996) 3177–3184. <https://doi.org/10.1111/j.1151-2916.1996.tb08093.x>.
- [7] S.H. Chi, Specimen size effects on the compressive strength and Weibull modulus of nuclear graphite of different coke particle size: IG-110 and NBG-18, *J. Nucl. Mater.* 436 (2013) 185–190. <https://doi.org/10.1016/j.jnucmat.2012.09.023>.
- [8] B.J. Marsden, M. Haverty, W. Bodel, G.N. Hall, A.N. Jones, P.M. Mummery, M. Treifi, Dimensional change, irradiation creep and thermal/mechanical property changes in nuclear graphite, *Int. Mater. Rev.* 61 (2016) 155–182. <https://doi.org/10.1080/09506608.2015.1136460>.
- [9] A. Hodgkins, T.J. Marrow, P. Mummery, B. Marsden, A. Fok, X-ray tomography observation of crack propagation in nuclear graphite, *Mater. Sci. Technol.* 22 (2006) 1045–1051. <https://doi.org/10.1179/174328406X114126>.
- [10] A. Hodgkins, T.J. Marrow, M.R. Wootton, R. Moskovic, P.E.J. Flewitt, Fracture behaviour of radiolytically oxidised reactor core graphites: a view, *Mater. Sci. Technol.* 26 (2010) 899–907. <https://doi.org/10.1179/026708309X12526555493477>.
- [11] J. Marrow, A. Hodgkins, M. Joyce, B.J. Marsden, Damage nucleation in nuclear graphite, *Energy Mater.* 1 (2006) 167–170. <https://doi.org/10.1179/174892406x160651>.
- [12] M. Mostafavi, S.A. McDonald, P.M. Mummery, T.J. Marrow, Observation and quantification of three-dimensional crack propagation in poly-granular graphite, *Eng. Fract. Mech.* 110 (2013) 410–420. <https://doi.org/10.1016/j.engfracmech.2012.11.023>.

- [13] M. Mostafavi, S.A. McDonald, H. Çetinel, P.M. Mummery, T.J. Marrow, Flexural strength and defect behaviour of polygranular graphite under different states of stress, *Carbon*. 59 (2013) 325–336. <https://doi.org/10.1016/j.carbon.2013.03.025>.
- [14] R. Moskvic, P.J. Heard, P.E.J. Flewitt, M.R. Wootton, Overview of strength, crack propagation and fracture of nuclear reactor moderator graphite, *Nucl. Eng. Des.* 263 (2013) 431–442. <https://doi.org/10.1016/j.nucengdes.2013.05.011>.
- [15] Y. Vertyagina, T.J. Marrow, Multifractal-based assessment of Gilsocarbon graphite microstructures, *Carbon*. 109 (2016) 711–718. <https://doi.org/10.1016/j.carbon.2016.08.049>.
- [16] S.M. Barhli, L. Saucedo-Mora, M.S.L. Jordan, A.F. Cinar, C. Reinhard, M. Mostafavi, T.J. Marrow, Synchrotron X-ray characterization of crack strain fields in polygranular graphite, *Carbon*. 124 (2017) 357–371. <https://doi.org/10.1016/j.carbon.2017.08.075>.
- [17] D. Liu, B. Gludovatz, H.S. Barnard, M. Kuball, R.O. Ritchie, Damage tolerance of nuclear graphite at elevated temperatures, *Nat. Commun.* 8 (2017) 1–9. <https://doi.org/10.1038/ncomms15942>.
- [18] R. Krishna, J. Wade, A.N. Jones, M. Lasithiotakis, P.M. Mummery, B.J. Marsden, An understanding of lattice strain, defects and disorder in nuclear graphite, *Carbon*. 124 (2017) 314–333. <https://doi.org/10.1016/j.carbon.2017.08.070>.
- [19] J.H.W. Simmons, *Radiation Damage in Graphite*, Elsevier, Glasgow, UK, 1965. <https://doi.org/10.1016/C2013-0-05555-7>.
- [20] R.E. Nightingale, *Nuclear Graphite*, 1st ed., Academic Press, New York, 1962.
- [21] T.D. Burchell, Fission Reactor Applications of Carbon, in: T.D. Burchell (Ed.), *Carbon Mater. Adv. Technol.*, 1st ed., Elsevier, Oxford, UK, 1999: pp. 429–484. <https://doi.org/10.1016/B978-008042683-9/50015-7>.
- [22] R.J. Price, Strength of Irradiated Graphite: a Review, in: *Meet. Mech. Behav. Graph. High Temp. React.*, Gif-sur-Yvette, France, 1979: pp. 69–76.
- [23] T.D. Burchell, W.P. Eatherly, The effects of radiation damage on the properties of GraphNOL N3M, *J. Nucl. Mater.* 179–181 (1991) 205–208. [https://doi.org/10.1016/0022-3115\(91\)90062-C](https://doi.org/10.1016/0022-3115(91)90062-C).
- [24] T.D. Burchell, L.L. Snead, The effect of neutron irradiation damage on the properties of grade NBG-10 graphite, *J. Nucl. Mater.* 371 (2007) 18–27. <https://doi.org/10.1016/j.jnucmat.2007.05.021>.
- [25] A.A. Campbell, Y. Katoh, M.A. Snead, K. Takizawa, Property changes of G347A graphite due to neutron irradiation, *Carbon*. 109 (2016) 860–873. <https://doi.org/10.1016/j.carbon.2016.08.042>.
- [26] S. Sato, A. Kurumada, K. Kawamata, T. Takizawa, K. Teruyama, Neutron irradiation effects on thermal shock resistance and fracture toughness of graphites as plasma-facing first wall components for fusion reactor devices, *Carbon*. 27 (1989) 507–516.

- [https://doi.org/10.1016/0008-6223\(89\)90001-8](https://doi.org/10.1016/0008-6223(89)90001-8).
- [27] T.D. Burchell, J.P. Strizak, The effect of neutron irradiation on the fracture toughness of graphite, *Nucl. Eng. Des.* 271 (2014) 262–269.  
<https://doi.org/10.1016/j.nucengdes.2013.11.046>.
  - [28] A. Tzelepi, P. Ramsay, A.G. Steer, J. Dinsdale-Potter, Measuring the fracture properties of irradiated reactor core graphite, *J. Nucl. Mater.* 509 (2018) 667–678.  
<https://doi.org/10.1016/j.jnucmat.2018.07.024>.
  - [29] G. Haag, Properties of ATR-2E Graphite and Property Changes due to Fast Neutron Irradiation, Jülich, 2005. [http://juser.fz-juelich.de/record/49235/files/Juel\\_4183\\_Haag.pdf](http://juser.fz-juelich.de/record/49235/files/Juel_4183_Haag.pdf).
  - [30] N. Tzelepi, J. Dinsdale-Potter, M. Jordan, H. Preston, G. Copeland, M. Crelling, T. McGrady, S. Wilkinson, P. Ramsay, Innovate-UK Project: Influence of Creep and Geometry on Strength of Irradiated Graphite Components - Work Package 1: Measurements of Strength and Fracture Properties on Irradiated Graphite, Sellafield, UK, 2017.
  - [31] L. Shi, H. Li, Z. Zou, A.S.L. Fok, B.J. Marsden, A. Hodgkins, P.M. Mummery, J. Marrow, Analysis of crack propagation in nuclear graphite using three-point bending of sandwiched specimens, *J. Nucl. Mater.* 372 (2008) 141–151.  
<https://doi.org/10.1016/j.jnucmat.2007.02.012>.
  - [32] P.J. Heard, M.R. Wootton, R. Moskovic, P.E.J. Flewitt, Crack initiation and propagation in pile grade A (PGA) reactor core graphite under a range of loading conditions, *J. Nucl. Mater.* 401 (2010) 71–77. <https://doi.org/10.1016/j.jnucmat.2010.03.023>.
  - [33] T.H. Becker, T.J. Marrow, R.B. Tait, Damage, crack growth and fracture characteristics of nuclear grade graphite using the Double Torsion technique, *J. Nucl. Mater.* 414 (2011) 32–43.  
<https://doi.org/10.1016/j.jnucmat.2011.04.058>.
  - [34] C.G. Sammis, M.F. Ashby, The failure of brittle porous solids under compressive stress states, *Acta Metall.* 34 (1986) 511–526. [https://doi.org/10.1016/0001-6160\(86\)90087-8](https://doi.org/10.1016/0001-6160(86)90087-8).
  - [35] C. Tang, J.A. Hudson, *Rock Failure Mechanisms Explained and Illustrated*, 1st ed., CRC Press, Boca Raton, FL, 2010.
  - [36] C.M. Cady, C. Liu, M.L. Lovato, Determination of dynamic fracture toughness using a new experimental technique, *EPJ Web Conf.* 94 (2015) 01012.  
<https://doi.org/10.1051/epjconf/20159401012>.
  - [37] C.M. Cady, D.E. Eastwood, N.K. Bourne, C. Liu, R. Pei, P. Mummery, W. Bodel, J. Wade, R. Krishna, S. Cipiccla, A.J. Bodey, K. Wanelik, C. Rau, Fundamental considerations in fracture in nuclear materials, in: *AIP Conf. Proc.* 1979, 2018: p. 070009.  
<https://doi.org/10.1063/1.5044818>.
  - [38] G.E. Bacon, A method for determining the degree of orientation of graphite, *J. Appl. Chem.* 6 (1956) 477–481. <https://doi.org/10.1002/jctb.5010061101>.
  - [39] A.A. Campbell, K.B. Campbell, G.S. Was, Anisotropy analysis of ultra-fine grain graphite and

- pyrolytic carbon, *Carbon*. 60 (2013) 410–420. <https://doi.org/10.1016/j.carbon.2013.04.054>.
- [40] A.J. Bodey, Z. Mileeva, T. Lowe, E. Williamson-Brown, D.S. Eastwood, C. Simpson, V. Titarenko, A.N. Jones, C. Rau, P.M. Mummery, Simultaneous heating and compression of irradiated graphite during synchrotron microtomographic imaging, *J. Phys. Conf. Ser.* 849 (2017) 012021. <https://doi.org/10.1088/1742-6596/849/1/012021>.
- [41] C. Rau, U. Wagner, Z. Pešić, A. De Fanis, Coherent imaging at the Diamond beamline I13, *Phys. Status Solidi*. 208 (2011) 2522–2525. <https://doi.org/10.1002/pssa.201184272>.
- [42] Z.D. Pešić, A. De Fanis, U. Wagner, C. Rau, Experimental stations at I13 beamline at Diamond Light Source, *J. Phys. Conf. Ser.* 425 (2013) 182003. <https://doi.org/10.1088/1742-6596/425/18/182003>.
- [43] M. Basham, J. Filik, M.T. Wharmby, P.C.Y. Chang, B. El Kassaby, M. Gerring, J. Aishima, K. Levik, B.C.A. Pulford, I. Sikharulidze, D. Sneddon, M. Webber, S.S. Dhesi, F. Maccherozzi, O. Svensson, S. Brockhauser, G. Náray, A.W. Ashton, Data Analysis WorkbeNch ( DAWN ), *J. Synchrotron Radiat.* 22 (2015) 853–858. <https://doi.org/10.1107/S1600577515002283>.
- [44] V. Titarenko, R. Bradley, C. Martin, P.J. Withers, S. Titarenko, Regularization methods for inverse problems in x-ray tomography, in: S.R. Stock (Ed.), 2010: p. 78040Z. <https://doi.org/10.1117/12.860260>.
- [45] J. Schindelin, I. Arganda-carreras, E. Frise, V. Kaynig, M. Longair, T. Pietzsch, S. Preibisch, C. Rueden, S. Saalfeld, B. Schmid, J. Tinevez, D.J. White, V. Hartenstein, K. Eliceiri, P. Tomancak, A. Cardona, Fiji : an open-source platform for biological-image analysis, 9 (2019). <https://doi.org/10.1038/nmeth.2019>.
- [46] D. Liu, P.E.J. Flewitt, Deformation and fracture of carbonaceous materials using in situ micro-mechanical testing, *Carbon N. Y.* 114 (2017) 261–274. <https://doi.org/10.1016/j.carbon.2016.11.084>.
- [47] P.J. Heard, M.R. Wootton, R. Moskovic, P.E.J. Flewitt, Deformation and fracture of irradiated polygranular pile grade A reactor core graphite, *J. Nucl. Mater.* 418 (2011) 223–232. <https://doi.org/10.1016/j.jnucmat.2011.07.003>.
- [48] S. Fazluddin, Crack growth resistance in nuclear graphites, The University of Leeds, 2002.
- [49] T.J. Marrow, D. Liu, S.M. Barhli, L. Saucedo Mora, Y. Vertyagina, D.M. Collins, C. Reinhard, S. Kabra, P.E.J. Flewitt, D.J. Smith, In situ measurement of the strains within a mechanically loaded polygranular graphite, *Carbon*. 96 (2016) 285–302. <https://doi.org/10.1016/j.carbon.2015.09.058>.
- [50] S. Sato, S. Miyazono, Studies of elastic modulus of irradiated graphite by an ultrasonic pulse method, *Carbon*. 2 (1964) 103–114. [https://doi.org/10.1016/0008-6223\(64\)90049-1](https://doi.org/10.1016/0008-6223(64)90049-1).
- [51] C. Karthik, J. Kane, D.P. Butt, W.E. Windes, R. Uvic, Neutron irradiation induced microstructural changes in NBG-18 and IG-110 nuclear graphites, *Carbon*. 86 (2015) 124–131.

- <https://doi.org/10.1016/j.carbon.2015.01.036>.
- [52] H.M. Freeman, A.N. Jones, M.B. Ward, F.S. Hage, N. Tzelepi, Q.M. Ramasse, A.J. Scott, R.M.D. Brydson, On the nature of cracks and voids in nuclear graphite, *Carbon*. 103 (2016) 45–55. <https://doi.org/10.1016/j.carbon.2016.03.011>.
  - [53] L. Babout, P.M. Mummery, T.J. Marrow, A. Tzelepi, P.J. Withers, The effect of thermal oxidation on polycrystalline graphite studied by X-ray tomography, *Carbon*. 43 (2005) 765–774. <https://doi.org/10.1016/j.carbon.2004.11.002>.
  - [54] Y. Vertyagina, T.J. Marrow, A multi-scale three-dimensional Cellular Automata fracture model of radiolytically oxidised nuclear graphite, *Carbon*. 121 (2017) 574–590. <https://doi.org/10.1016/j.carbon.2017.06.031>.
  - [55] C.I. Contescu, J.D. Arregui-Mena, A.A. Campbell, P.D. Edmondson, N.C. Gallego, K. Takizawa, Y. Katoh, Development of mesopores in superfine grain graphite neutron-irradiated at high fluence, *Carbon*. 141 (2019) 663–675. <https://doi.org/10.1016/j.carbon.2018.08.039>.
  - [56] S.-K. Seo, J.-S. Roh, S.-H. Kim, S.-H. Chi, E.-S. Kim, Thermal Emissivity of Nuclear Graphite as a Function of its Oxidation Degree (3): Structural Study using Scanning Electron Microscope and X-Ray Diffraction, *Carbon Lett.* 12 (2011) 8–15. <https://doi.org/10.5714/cl.2011.12.1.008>.
  - [57] Z.Y. Deng, J. She, Y. Inagaki, J.F. Yang, T. Ohji, Y. Tanaka, Reinforcement by crack-tip blunting in porous ceramics, *J. Eur. Ceram. Soc.* 24 (2004) 2055–2059. [https://doi.org/10.1016/S0955-2219\(03\)00365-0](https://doi.org/10.1016/S0955-2219(03)00365-0).
  - [58] T.D. Burchell, A microstructurally based fracture model for polygranular graphites, *Carbon N. Y.* 34 (1996) 297–316. [https://doi.org/10.1016/0008-6223\(95\)00171-9](https://doi.org/10.1016/0008-6223(95)00171-9).



